IEEE Access
Multidisciplinary ⋮ Rapid Review ⋮ Open Access Journal

Received 5 September 2022, accepted 26 September 2022, date of publication 3 October 2022,
date of current version 11 October 2022.

Digital Object Identifier 10.1109/ACCESS.2022.3211319

RESEARCH ARTICLE

WearROBOT: An Energy Conservative Wearable Obstacle Detection Robot With LP Multi-Commodity Graph

KENNEDY CHINEDU OKAFOR[1,2], (Senior Member, IEEE), AND OMOWUNMI MARY LONGE[2], (Senior Member, IEEE)
[1]Department of Mechatronics Engineering, Federal University of Technology-Owerri, Owerri 1526, Nigeria
[2]Department of Electrical and Electronic Engineering Science, University of Johannesburg, Johannesburg 2006, South Africa

Corresponding author: Kennedy Chinedu Okafor (kennedy.okafor@futo.edu.ng)

This work was supported in part by the Tetfund Nigeria under Grant TETF/ES/UNIV/IMO STATE/TSAS/2021.

ABSTRACT Human activity wearable obstacle detection for the visually impaired (VI) was developed for routine monitoring and observation of surrounding events. Environmental observation, home surveillance, and assistive supports are now built on wearable devices using inertia-based sensors, such as accelerometers, linear acceleration, and gyroscopes. However, previous assisted living system (ALS) still faces challenges in energy management and resource allocation when performing daily activities, particularly with ambulation. Legacy systems cannot fully improve self-esteem, hence, WearROBOT, which detects rearview obstacles and has an audio feedback system incorporated for voicing out once an obstacle is detected. Linear programing (LP) multi-commodity graph (LMCG) learning model is proposed while coupling the shortest path resource allocation for space diversity linearization. An Infrared sensor problem function that minimizes link utilization is derived. Angle-Intensity analysis (AIA) was carried out on various use case scenarios to enable the user to know the best angle to consider depending on its usage and battery conservation. This work showed how intensity differs at various angles of 5°, 15°, 20°, 35°, and 45°. Also, the reflectivity of different materials and how it affects the battery life are studied. As the wearable robot moves away from the node-obstacle, the LMCG narrow-band sensor node (LMCG-NB-IoT) drops energy significantly. The Low Power WAN (LP-WAN), Bluetooth Low-Energy (BLE) and proposed LMCG-NB-IoT offered 51.28%, 33.33%, and 15.39% respectively. In terms of energy latency, the schemes gave 65.63%, 31.25%, and 3.12% respectively. Similarly, the proposed LMCG-NB-IoT had a 50% battery life profile. Finally, WearROBOT mobility aid minimizes injuries experienced by the visually impaired.

INDEX TERMS Artificial intelligence, assisted living systems, machine learning, robotics, embedded systems.

I. INTRODUCTION

The field of future wearable robotics is rapidly changing especially in terms of human-robot interaction (HRI). Assisted living communities are growing globally. According to the latest world health organization (WHO) report, about 2.2 billion people globally are suffering from a near- or distance vision impairment [1]. Nearly half of these cases, or at least 1 billion, are caught up with vision damage that could have been avoided or fully unaddressed with smart wearable technologies. From the report, yearly costs associated with productivity losses are linked to visual impairment (VI). This is attributed to untreated myopia and presbyopia among other factors. The cost is estimated to be US$ 244 billion and US$ 25.4 billion, respectively. Therefore, the VI places a significant financial burden on the entire world [1]. The only solution is centered on disruptive technologies such as the Ambient Assisted Living system (AALS). This concept seems to have drawn attention due to its wide range of benefits in modern times [2], [3], [4]. The advancements in

The associate editor coordinating the review of this manuscript and approving it for publication was Okyay Kaynak.

technology especially artificial intelligence, IoT, and analytics have equally contributed to the growth trend [5], [6], [7]. These systems make extensive use of smart devices to support older and disabled persons to stay safe and healthy in their environments.

The usual component of ASL systems includes smart-sensing devices, wireless sensing/IoTs, analytic software, and medical sensing tools [7]. This makes aging less complicated. In most cases, the visually impaired mostly use mobility aids during ambulation. The mobility aids (traditional and electronic) provide different functionalities such as detection of obstacles, drop-offs, overhanging obstacles, potholes, and elevation among others [9], [10], [8], [11], [12], [13], [14].

Existing electronic mobility aids for the visually impaired and deaf person (such as - white cane, snow guard, miniguide, sonic pathfinder, tom pouce, smart cane, intelligent walking stick, and ultrasonic cane), are limited in their attributes and functionalities [15]. Though the highlighted types provide the above-listed functionalities, detection on the rear side is not feasible, especially in a community of limited vision persons. Also, these do not provide additional information about the direction of the obstacle. Again, battery life, miniaturization of the aid, and obstacle proximity alert remain unsolved issues in the existing mobility aids.

The major driving motivation accelerating AALS in most countries is government policy on disruptive technologies [16]. This has been made compulsory for assisting the aging and disabled population [17], [18]. The ease of monitoring and control systems has triggered the smart electronic gadget market segment. These can be linked to cloud-based applications, home devices, etc. In the community of the limited vision, AALS will provide massive support for the limited vision and visually impaired. Graph theory has been seriously applied in Chemical Graph Theory [19], drug-naïve obsessive-compulsive disorder [20], non-human primates [21], and other smart health domains [22], [23].

This research has significance to society considering the increasing number of the visually impaired globally [24]. Existing mobility aids have limitations especially in transmitting energy conservation during mobility. Hence, there is a need to design an efficient and reliable mobility aid that would address current limitations.

With the LP multi-commodity graph, signal transmissions under energy conservation are realized. An audio feedback graph will be used to detect the direction of the obstacle, thereby giving additional information about the environment. Furthermore, one of the challenges faced by other electronic systems in use is the significant energy consumption, battery drops, and link connectivity issues. This work will provide an improved battery life performance with a much lower consumption rate. The implementation of the robot will significantly improve the self-esteem of the visually impaired by reducing their dependency level.

This paper focused on addressing the limitations of existing mobility aids, particularly in obstacle detection at the rear side and in real time. This helps to prevent back injuries, which cause a major threat to the visually impaired thereby reducing their functionality and, at the same time, increasing their standard of living.

A. RESEARCH CONTRIBUTIONS

This article aims at designing a resilient sensor-based wearable obstacle detector robot for the visually impaired using LP multi-commodity graph theory. The detector is based on the infrared sensor device implementation. The main contributions are summarized below:

- Formulation of an LP Multi-commodity graph for AALS.
- Determination of the optimal sensor placement position that would facilitate the detection of rear-side, front-side, right-side, and left-side obstacles.
- Design of a miniaturized wearable obstacle detector architecture using an infrared sensor.
- Integration of scalable transducer feedback routine into the wearable obstacle detector system.
- Performance evaluation considering energy consumption, energy latency, battery life performance, reflectivity, and span distances.

This article highlights the design concepts as found in AAL systems, embedded implementation schemes, and graph theory applications. The evaluation of mobility aid for the visually impaired is discussed. Use case optocoupler, secure digital card (SD card), audio system, vibrator, buzzer, and PIC16F876A microcontroller are explored. The system can be integrated into aids for the physically and mentally challenged such as wheelchairs, prosthetic limbs, Zimmer walking frames, and crutches, but these are outside the scope of this work.

The rest of this paper is organized as follows. Section II presents related works. Section III reported the optimization model. Section IV discussed the WearROBOT algorithms and computational complexity. Section V discussed the proof-of-concept validation. Section VI discussed Simulation Analysis. Section VII addressed performance validations. Section VIII concludes the paper with future works.

II. RELATED WORKS

This section focused on related works in ALS efforts, and embedded node capabilities. Also, a systematic literature review (SLR) is used to establish foundations for WearROBOT in this research.

A. EFFORTS ON ASSISTED LIVING SYSTEMS

There have been various efforts in AALS for the visually impaired (the limited vision) to detect obstacles beyond knee level at a long-range and in real-time using radio frequency identification [11]. Also, common obstacle detection techniques are elucidated, self-attention model, [13], [25]. Physical disability has been a major setback to individuals, their families, and subsequently, national development. Visual impairment is a major physical challenge that has rendered

many helpless. The authors [11], presented an assisted glove device that supports the visually impaired to interact with their environments. The work [12] focused on a smart assistive machine with emphasis on wearable smart glasses including a motion stick for the visually impaired (VI). This was used to detect aerial obstacles and falls. In [13], the authors proposed an assistive module for the VI that explores more dimensional data to identify objects. The research converts 3-D spatial information into sound details using 6-axis and ultrasonic sensors while drawing a 3-D space image for the user. In paper [14], the authors discussed the implementation of a unit-cell electromagnetic refreshable braille display that can be read by the VI or the limited vision. The authors in [15] proposed a monocular vision-based system for assisted living, especially for persons that needs help during ambulation (i.e., in-outdoor, and outdoor places). The authors in [26] also proposed a fully latching and scalable haptic display system that conveys dynamic graphical information to the limited vision/VI. In [27], assistive technology- Cardbot 2.0 was introduced as a learning aid for the VI. Similarly, a haptic AT was developed for the visually impaired considering Braille reading, tactile graphics, orientation, and mobility [28]. Other related efforts were studied including the applications of Gaussian hidden Markov model [29], locomotion recognition algorithm [30], three-dimensional (3D)-printed multifunctional hand device (3DP-MFHD) [31], eye-tracking assistive [32], and unsupervised sim-to-real adaptation [33]. The major gap is that most works lack details on the effect of angle positioning on distance while keeping the energy absorbed constant. Hence, energy management is yet to be fully unresolved in smart wearable devices.

B. ASSISTED LIVING NODE CAPABILITIES

Most assisted living wearable systems have issues with energy conservation. Various analytical models have been reported to address power drain concerns in AALS [34]. Most of the works are based on IoT, which naturally has power limitations [7], [35]. Also, there are experimental investigations carried out to distinctly evaluate localized metrics such as energy consumption [34], node capacity, sensing scalability [36], prediction accuracy [25], node-to-node communication [37], and security [38]. The commonality in several existing studies is that one or more technologies are focused upon in their discussions.

A comparative study of various results considering most works in literature may hardly offer an insightful and balanced perspective since each experimental model is carried out using baseline assumptions varying in several optical landscapes by these authors. Lately, there are very few works involving more than three technologies. However, the work [34] compared wearable IoT performance with GPRS [39], Bluetooth [40], and NB-IoT [41] with Sigfox [42] and LoRa [43], [44]. The scarcity of graph-based literature in the previous studies suggests the need for more efforts in lightweight multi-commodity graph theory. Recent reviews of wearable robots are summarized in Table 1 based on their areas of focus. Many of the works focused on single technologies while energy consumption and graph optimization were not considered in most of the studies. However, looking at the significance of narrowband IoT-powered wearables in context, it is critical to consider graph-based energy performance in literature. One of the areas of investigation is the positional angles, energy consumption, and how the surface of the material affects the absorption rate.

Most works in literature failed to emphasize these areas in wearable AALs. The closest efforts in wearable dynamic sensor selection activity recognition have been discussed. Preprocessing, feature extraction, and classification are critical in obstacle sensing. Sleep state in activity recognition, active classification of sensed obstacles, and energy faulty states lack empirical evidence as well as theoretical perspectives.

A closer look at Gaussian Hidden Markov Model (GHMMs) offers good insights into obstacle identification via data aggregation [45]. Their parametric learning design is based on a maximization algorithm that leverages collective Gaussian Forward-Backward algorithm. Another good work on wearable sensor algorithms was presented in [46]. In their work, sensor-based wearable devices explored machine learning to achieve posture-triggered detection and real-time activity recognition. The efforts involve raw data machine learning computation while reducing computational costs and latency. Also, Multi-Mapping Spherical Normalization (MMSN) was applied in obstacle detection and classification Support Vector Machine (SVM) with Radial Basis Function Kernel (RBF-SVM). This addressed computational complexity and accuracy while considering energy conservation on wearable nodes.

C. MULTI-DIMENSIONAL GRAPH-BASED COMPUTING

In a wearable sensor network (WSN), optimal capacity analysis is needed for energy conservation. Multi-radio-multi-channel WSN intrinsically demands mixed integer program multi-radio formulation [47]. This is an NP-hard problem found in most recent heuristic algorithms such as the Gaussian mixture model (GMM), and multi-dimensional conflict graph (MDCG). Trajectory planning has been addressed with MDCG while capacity optimization concerns have been accurately dealt with using linear programming (LP) multi-commodity flow (MCF) problem [48]. These schemes have been optimized with maximal independent constraints. The MDCG-based offering gives maximum throughput and optimal configurations on routing, channel assignment, and scheduling in complex WSNs. Also, MDCG-based optimal capacity planning uses dynamic channel swapping. As an improvement, the proposed LMCG offers better obstacle sensing capability, which is challenging to achieve in existing heuristic algorithms. In this article, the proposed LMCG offers polynomial computing based on the shortest-path scheduling in obstacle detection.

The central concept of this article is on the wearable sensor node module. It discussed an energy conservative wearable obstacle detection robot that detects rear view obstacles with

an audio feedback system incorporated for voicing out once an obstacle is detected. A LMCG learning model is proposed while coupling the shortest path resource allocation for space diversity linearization considering the wearable sensor nodes that makes this obstacle detection for the visually impaired. The various domain applications, contributions, and gaps analysis are summarized in Table 1.

Now, let's define a major design concern. To minimize average signal package delays, there is a need to optimize the max link utilization in the space diversity domain.

III. OPTIMIZATION MODEL

In this section, this article formulates the Infrared sensor problem function that minimizes link utilization considering traffic demand $\boldsymbol{h_d}(\mathbf{1}, \mathbf{2}, \ldots \boldsymbol{D})$ and capacity $\boldsymbol{C_e}(\boldsymbol{e} = \mathbf{1}, \mathbf{2}, \ldots .., \boldsymbol{E})$. Also, a routing algorithm is mapped with an open shortest path First (OSPF). Let's denote the link weight metric $\boldsymbol{e}$ with $\boldsymbol{\beta_e}$. This can assume a non-negative or positive value depending on the OSPF boundary for the IR sensor. This implies that the $\boldsymbol{\beta}(\boldsymbol{\beta_1}, \boldsymbol{\beta_2}, \ldots .., \boldsymbol{\beta_E})$ then pushes IR demand flow (traffic) for respective node demand using the OSPF routing scheme. The equal-cost multi-path (ECMP) rule applies when there are various available shortest paths for demand $\boldsymbol{d}$ making transmission flow split equally among the transmitter and the receivers. See Appendix I for notations.

Let's give the RF flow on path P for traffic demand d triggered with a link metric system β i.e., $xdp(\beta)$. This energy metric is important given the level of dependency of traffic flows on β based on OSPF. By summation convention, this gives (1).

$$\sum_p xdp\,(\beta) = h_d, \quad d = 1, 2, \ldots .D \tag{1}$$

In the link metric system β, let δ_{edp} represent the link-path indicator, which implies that it can assume a value of 1 if route p for demand d makes use of link e, else it uses 0. The flow link or link load y_{-e} on link e induced by β is given by (2).

$$y_{-e}(\beta) = \sum\nolimits_d \sum\nolimits_p e_{dp} x_{dp}\,(\beta), \quad e = 1, 2, \ldots \ldots .., E \tag{2}$$

Certainly, the flow- link will be capacity-bounded such that (3):

$$y_{-e}(\beta) \leq C_e, \quad e = 1, 2, \ldots \ldots ., E \tag{3}$$

The link utilization on each transmitter traffic link e is represented by (4):

$$y_{-e}(\beta)/C_e \tag{4}$$

The maximum utilization over all links depends on a variable (5):

$$\tau = Max_e = 1, \ldots \ldots \ldots ., E\,\{y_{-e}(\beta)/C_e.\} \tag{5}$$

In the system, the link with optimal. Maximum utilization is the link e where the ratio is highest (max congestion). The formulation of the objective function will be minimizing the link utilization of the sensors. This is obtained as follows (6):

$$\begin{aligned} &\underset{\boldsymbol{\beta}}{\boldsymbol{Minimize}}\ \boldsymbol{F} = Max_e \left\{ \left\{ \frac{y_{-e}\,(\beta)}{C_e}. \right\} \right\} \\ &\boldsymbol{S.t}\ \sum\nolimits_p xdp\,(\beta)\,, = h_d \quad d = 1, 2, \ldots .D \\ &\quad \sum\nolimits_d \sum\nolimits_p \delta_{edp} x_{dp}\,(\beta) = y_{-e}\,(\beta) \quad e = 1, 2, ..E \\ &\quad y_{-e}(\beta) \leq C_e, \quad e = 1, 2, ..E \\ &\quad \boldsymbol{\beta_e}\ \text{Non-negative integers} \end{aligned} \tag{6}$$

Considering the above formulation, the link metric variables can be modified with an auxiliary variable $\boldsymbol{\tau}$ to remove the link load equation in the previous formulation.

$$\begin{aligned} &\underset{\boldsymbol{\beta}, \boldsymbol{\tau}}{\boldsymbol{Minimize}}\ \boldsymbol{F} = \boldsymbol{\tau} \\ &\boldsymbol{S.t}\ \sum_p xdp\,(\beta)\,, = h_d \quad d = 1, 2, \ldots .D \\ &\quad \sum_d \sum_p \delta_{edp} x_{dp}\,(\beta) \leq C_e \boldsymbol{\tau} \quad e = 1, 2, ..E \\ &\quad \boldsymbol{\tau}\ \text{continuous} \\ &\quad \boldsymbol{\beta_e}.\text{Non-negative integers} \end{aligned} \tag{7}$$

From the above formulation (7), there will be zero link congestion if the optimal $\boldsymbol{\tau}^* < 1$. This is used to develop a sensor optimal algorithm that determines the appropriate optimal link-metric system β. The algorithm I then help to compute β considering traffic volume capacity and energy dissipation. The idea is to have the relaxed routing removed from (7) especially when independent decision variables xdp are used rather than β and $xdp(\beta)$. Such LP multi-commodity flow context can reduce optimal objective $\boldsymbol{\tau}^*$. Again, the weighted metric β influences the imposition of constraints states on the link flows.

Let's now discuss the system weight optimization problem. Given that once the link capacity C_e is provided a Poisson distribution arrival rate y_{-e} pps. The RF packet length has exponential distribution, and this gives an average energy packet delay in (8).

$$A_{pd} = {}^1\!/_{(C_e - y_{-e})} \tag{8}$$

This is done according to the $M/M/1$ queuing model. It is referred to as the latency function of the link e. For the link capacity connected workload, capacity demand is given by (9).

$$y_{-e} \leq C_e - {}^1\!/_T \tag{9}$$

Hence, the weighted-dependent optimal network objective is met with (9). Here, the NP-Completeness for the shortest-path routing assignment problem must be sufficiently satisfied. But let's further investigate the formulated theoretical context for the RF shortest-path link allocation challenge in WearROBOT architecture in Appendix II.

Proposition 1: Problems of Link Path Formulation for shortest path routing/bounded link delay (i.e., energy latency) need to be highlighted and proved.

TABLE 1. Summary of related work.

Ref	Focus area	Contribution	Energy conservation	Limitations/Gaps
[49]	Multi-robot image recognition system	Graph Neural Network Inference Perception	None	Focused on multi-view visual perception with limited parameter computation
[50]	Wearable Devices - Review Domain	Systematic reviews on the integration of sensor-based and computer vision-based technologies	None	Absence of graph computation and energy analysis.
[51]	Wearable StereoPilot	Impact object recognition	None	Unclear user experience for the Blind Visually Impaired
[52]	Smart Assisted Living System	Injection of Viola-Jones and TensorFlow Object Detection algorithm	None	Use of ultrasonic sensor mounted on a servomotor to measure the distance between the blind person and obstacles without graph computation
[53]	Visual Aid Assisted Living System	Lightweight, portable &, and controlled environment for visual aid system for the completely blind	None	Little analysis on visual aid system deployment and zero energy management schemes
[12]	Assistive Living System	Mobile device app, with a cloud-based management platform	None	Absence of graph computation and energy analysis.
[54]	Optimal Assistive System	Visual Odometry deployment	None	Analysis of average accuracy, sensitivity, and specificity without graph computation and energy analysis.
[55]	Assistive system	Convolutional NN adaptation on big data	None	Obstacle detection with unclear cloud computational algorithm.
[56]	Deep Assisted Living System	Semantic obstacle categorization	None	Absence of graph computation and energy analysis
	Proposed WearROBOT	Energy conservation and optimal link utilization for obstacle detection.	Yes	Cost overhead due to lightweight optimal sensor placement with lower computational overhead

Proof: Imagine the directed WearROBOT single-commodity flow graph in Figure 1. The vertex $\boldsymbol{\mu s}$ is the source transmitter, and the vertex $\boldsymbol{\mu t}$ is the sink. Also, the vertices in the mapped upper row represent the 3-sets of family C while those at the lower row correspond to the elements of set X. The edges between the two rows reflect the incidence relation between family C and set X. Vertex C_i is connected to vertex x_k if and only if $x_k \in C_i$, i.e., $C_1 = \{x_1, x_2, x_3\}$, $C_2 = \{x_2, x_4, x_k\}$ and $C_n = \{x_{k-1}, x_{k+1}, x_p\}$. The new assumption is that $X \subseteq C$.

The source vertex $\boldsymbol{\mu s}$ and the sink vertex $\boldsymbol{\mu t}$ are shown in Figure 1 depicting the graph transactions. The physical architecture is shown in Appendix II.

In Figure 2, the maximal flow from vertex μs to vertex μt could be described in polynomial time. Assuming IR subfamily $C^{\wedge} = \{C_{i(1)}, C_{i(2)}, \ldots..C_{i(q)}, \}$ houses link state set$X$. By assigning flows $=1$ to all edges $(s, C_{i(j)})$ *for* $j = 1, 2, \ldots\ldots q(i.e., f(s, C_{i(j)} = 1, j = 1, 2, \ldots\ldots q)$, and flow $= 0$ to the rest of the edges of the form (s, C_l). This state allocation will compel $f(x_k, u) = 1/3$ for $k = 1, 2, \ldots..p$. Finally, by assuming $f(s, t) = 1$, this makes ECMP flow with a value of $q+1$. The edges are saturated incoming to vertex u. The vertices C_l with $f(s, C_l) = 1$ defines the family C covering X. Hence, by finding ECMP flow $= q + 1$, this verifies NP-completeness found in ECMP flow problem.

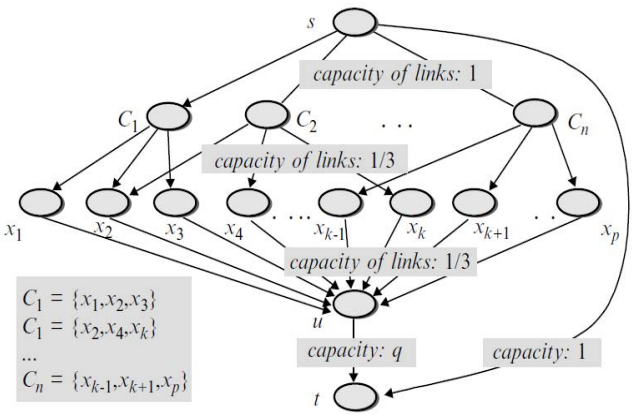

FIGURE 1. WearROBOT RF multi-commodity flow graph.

IV. WearROBOT ALGORITHMS AND COMPUTATIONAL COMPLEXITY

In this section, WearROBOT shortest-path problem is solved by modifying Dijkstra's algorithm [57], [58]. The idea is to allow the IR transmitter to identify the least administrative

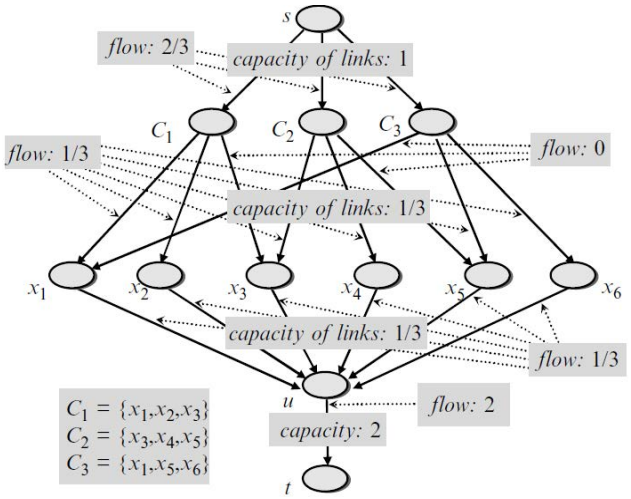

FIGURE 2. WearROBOT single-commodity flow graph instance.

path starting from source to sink in a community of wearable nodes. For sensor-based data gathering, Reliable Path Selection and Opportunistic Routing (RPSOR) [59], software-defined networking, Fog/edge IoT systems [57], [60], [61] have extensively explored the Dijkstra routing algorithm.

For a distance vector L and predecessor vector P, let's use a designated distance set and predecessors' vectors L_i and P_i $(i = 1, 2 \ldots n)$.

The $L_i(v)$ harvest the updated shortest path from source to sink at most active i jump. P_i $(i = 1, 2 \ldots n)$ and Pi(v) houses the previous vertex v on the recent closes path having at least i jumps. The computational algorithm uses clustered node-set, ψ which refers to the set pairs (v, i) (i.e., v is not labeled at level $i \leq i \leq n$). Here, $L_i(\mathrm{v}) < \infty$ in a way that vertex v could be linked from IR source s without middle deviations at the vertices. The algorithm I use vectors L and P with a set of labeled vertices C and X. Each entry $L(v)$ contains the distance measured from s to t along the current shortest path, while each entry $P(x_p)$ contains the parent of vertex v, i.e., the vertex from which vertex C has been reached (labeled) during the construction of the shortest path. Vector u is used at the last stage of the procedure to restore the constructed shortest path ($\oplus$ is the concatenation operator). Upon completion, $L(t)$ is equal to the length of the shortest path, P from s to t. Note that when the narrow band IR sensor needs the least administrative distance path from s to all available graph vertex. Without loss of generality, we can modify the algorithm by changing the status in the "*while statement*" using a similar line statement.

As shown in Dijkstra's Algorithm I, the sum vertices that could be energy conserved are $C(C-1)$ and $X(X-1)$. Hence, the complexity of the algorithm is $O(V^2)$. Advanced data structure design will minimize the complexity analysis to $O(E + Vlog\,(V)$. From Figure 1, the robot SPDA moves source S to destination t in the graph. The control routine terminates only if the destination sink t gets a label (i.e., moves into set S). The computational complexity of the considered variants in Algorithms I and II is then n times bigger than the complexity of the original algorithm. However, it is also less than $o(n \times V^2)$.

Algorithm 1: Modified WearROBOT Dijkstra's SPDA

1: **Procedure:** SPDA(G, s, t)
$S := \vartheta$; $t := \vartheta$; $L(s) := 0$;
For $S \in V|\{s\}$ *doL* $(v) := \infty$
While $t \notin S$ ***do*** ***(while*** $|S| < V$ ***do}***
Begin
$C_l := argMin\left\{\left\{C_{i(1)}, C_{i(2)}, \ldots..C_{i(q)}, \right\}\right\}$;
$\{S = \dot{V} \backslash S\}$
$t := argmin\left\{L\,(v) : v \in \dot{S}\right\}$; $\{S = \dot{V} \backslash S\}$
$S := S \cup \{v\}$;
$C_1 = \{x_1, x_2, x_3\}$, $C_2 = \{x_2, x_4, x_k\}$ &
$C_n = \left\{x_{k-1}, x_{k+1}, x_p\right\}$
for $\beta \in N(v) \cap \grave{S}$ ***do***
If $L\,(\beta) > L\,(v) + L_{vw}$; $P\,(w) := v$;
end
$P := (t)$; $v := t$;
Repeat
$v := P\,(v)$;
$P := v^{\circ}\emptyset \geq \oplus P$
until $v = \hat{S}$,
$SPDA := P$
end while
end {*procedure*}
Return

Algorithm II discussed the WearROBOT from closest paths having hop limit. This aspect of the IR nearest path challenge in the graph node is addressed by modifying Dijkstra's algorithm. The idea is to find the nearest RF path ℓ_e term) from the wearable transmitter s to respective sinks nodes within the signal paths for sink hops (i.e., edges). Algorithm II finds the nearest paths with active n jumps from source s to all other IR nodes. It comes back from s to an active sink t. In this scenario, we can avoid the vector L and p while using another set of L_i and $p_i(1, 2, 3 \ldots..n)$, where $L_i(v)$ houses the distance of the current closest path from s to v with active i link jumps. Also, rather than the set S of labeled vertices, for respective $i = 1, 2, 3 \ldots..n$, let's then create a set $\boldsymbol{S_i}$ labeled vertices tagged i, i.e., the set of vertices having the least administrative path that can connect any path IR node. In context, the algorithm used a conjugate set, $\boldsymbol{\mathcal{R}}$, (i.e., a set of all pairs (v, i). In this case, v is not labeled at level i. (note that $i \leq i \leq n$. This is convolved in a manner that gives $L_i\,(v) < \infty$. Similarly, the vertex v may be located from the source s in exactly i hops. Only actively assigned node transmitters can reach others using labeled vertices.

For the WearROBOT used in a limited vision community, a two-layer dimensioning problem is further considered for resource allocation in Algorithm III. Assuming the following additional considerations in a link formulation context.

Algorithm 2: Smartest-Path Dedicated Lower Hops (SPDLH)

1: **procedure:** *SPDLH* (G, s, t, n)
$\mathcal{R} := \{(v, 1) : v \in \mathbb{N}(s)\}$;
for $i := 1$ *to* n ***do*** $S_i := \{s\}$;
While $\boldsymbol{v} \notin \mathcal{R}$ ***do***
for $v = V(\mathbb{N}(s) \bigcup \{\}s)$ ***do***
for $i := 1$ *to* n ***do*** $L_i(v) ::= \infty$;
for $v \in \mathbb{N}(s)$ ***do***
for $i := 1$ *to* n ***do***
Begin $L_i(v) ::= L_{sv}$; $P_i(v) ::= s$ ***end***;
While $\mathcal{R} \neq 0$ ***do***
Begin
find $(\boldsymbol{v}, \boldsymbol{i}) \in \mathcal{R}$ such that:
(1) $\forall (\boldsymbol{w}, \boldsymbol{j}) \in \mathcal{R}, L_i(v) \leq L_j(w)$
(2) $\forall (\boldsymbol{w}, \boldsymbol{j}) \in \mathcal{R}, L_i(v) = L_j(w) \rightarrow j \geq i$;
$S_i := S_i \bigcup \{v\}$; $\mathcal{R} \backslash \{v, i\}$;
if $i >$ n ***then***

for $w \in \mathbb{N}(v) \cap (S_{i+1})'$ ***do*** $\{(S_{i+1})' = v(S_{i+1})\}$;
Begin

if $\boldsymbol{L_{iC1}}(\boldsymbol{w}) > L_i(v) + L_{vw}$ ***then*** $\mathcal{R} \cup (w, i+1))\}$
for $j := i + 1$ *to* n ***do***
Begin
$L_j(w) := L_{J-1}(v) + L_{vw}$; $P_{j(w)} := v$ ***end***;
end;
end;
$\boldsymbol{p} := (\boldsymbol{t})$; $\boldsymbol{v} := \boldsymbol{t}$; $\boldsymbol{i} := \boldsymbol{n}$;
repeat
$\boldsymbol{v} := P_i(v)$;
$\boldsymbol{p} := \boldsymbol{v} \oplus p$;
$\boldsymbol{i} := \boldsymbol{i} - 1$
Until $\boldsymbol{v} = \boldsymbol{s}$;
SPDLH $:= \boldsymbol{p}$
end while
end {*procedure*}
Return

Additional constants

$\mathfrak{M}$: the size of the IR node capacity in an upper location/layer
ξ_e: cost overhead on node capacity
ζ_{eq}: Unit capacity routing for graph node Variables
$\boldsymbol{x_{dp}}$: positive continuous RF flow allocated to path p
$\boldsymbol{y_e}$: positive integral node capacity.
$\boldsymbol{z_{eq}}$: positive RF flow/path allocation q for link capacity.

Objectives

$$\textbf{Minimize} \sum_{\boldsymbol{e}} \xi_e \boldsymbol{y_e} + \sum_{\boldsymbol{e}} \sum_{\boldsymbol{q}} \zeta_{eq} \boldsymbol{z_{eq}} \tag{10}$$

Constraints

$$\sum_{\boldsymbol{p}} \boldsymbol{x_{dp}} = \boldsymbol{h_d}, \quad d = 1, 2, \ldots\ldots.., D \tag{11}$$

$$\sum_{d} \sum_{p} \delta_{edp} x_{dp} \leq M_{y_e} \quad e = 1, 2 \ldots., E \tag{12}$$

$$\sum_{q} \boldsymbol{z_{eq}} = \boldsymbol{y_e}, \quad e = 1, 2, \ldots.E \tag{13}$$

$$\sum_{e} \sum_{q} \gamma_{geq} z_{eq} \leq c_g, \quad g = 1, 2, \ldots G \tag{14}$$

The above mode is crucial when the RF transport network for WearROBOT is considered in a non-invasive mode. In this case, the traffic network serves as the higher layer. The lower layer is dimensioned to transport signals across the various vertices. The IR sensor capabilities are leveraged to create multiple extended service sets for other connecting devices. All the nodes use Algorithm III to conserve link energy.

Algorithm 3: LCMG Flow Allocation (LFA)

procedure: *CPU controller*
LCMG_Allocation $(i, j, h_d, \mathbb{I}_{i,j})$
Given demands d with start Node i
End Node j and set of LFA paths $\widehat{\mathbb{P}_{i,j}}$
Begin $S_{ij} := \left\{e : e \text{ is first link of path } \mathcal{P} \in \widehat{\mathbb{P}_{i,j}}\right\}$;
find $(\boldsymbol{v}, \boldsymbol{i}) \in \mathcal{R}$ such that:
(1) $\forall (\boldsymbol{w}, \boldsymbol{j}) \in \mathcal{R}, L_i(v) \leq L_j(w)$
(2) $\forall (\boldsymbol{w}, \boldsymbol{j}) \in \mathcal{R}, L_i(v) = L_j(w) \rightarrow j \geq i$;
$S_i := S_i \bigcup \{v\}$; $\mathcal{R} \backslash \{v, i\}$;
if $i > n$ ***then***
for $w \in \mathbb{N}(v) \cap (S_{i+1})'$ ***do*** $(S_{i+1})' =$
$\widehat{\mathbb{P}_{i,j}} = \left\{e : e \text{ is first link of path } \mathcal{P} \in \widehat{\mathbb{P}_{i,j}}\right\}$;
//set of LFA paths but exclude link e
LCMG_Allocation$(i, j, h_d, \mathbb{P}_{i,j})$
Begin
end while
end {*procedure*}

V. PROOF OF CONCEPTS VALIDATION

A. PRELIMINARY DESIGN DESCRIPTION

In this subsection, the WearROBOT LMCG implementation was done using various materials and electronic devices including obstacle detection narrowband infrared sensor, microcontroller: PIC16F876A, vibrator, buzzer, audio system, LM 7805 voltage regulator, and secure digital (SD) Card in Figure 3. This obstacle detecting system uses the multi-modal graph for the visually impaired. This is accomplished using these steps:

STEP 1: The hardware components were developed ranging from sensor circuit, audio circuit, control unit, and memory unit, all built around a microcontroller.

STEP 2: Software development for the microcontroller was designed considering PIC16F876A. This is because of the ease of interfacing with other components and cost-effectiveness.

STEP 3: Testing was completed using agile-unit test scripts. The following are the specifications for WearROBOT.

i. WearROBOT energy consumption should not be more than 0.1 J. This will enable longer battery life and reduce energy quick battery replacements.
ii. Reflectivity: The reflectivity of the materials was put into consideration. The reason is that different surfaces offer different reflectivity. Also, quantity of energy absorbed differs for different materials. For instance, black objects absorb more energy than any other surface properties.
iii. Battery capacity, Size, and Weight: The higher the capacity, the bigger the size of the device and the greater the area occupied by the device. Nokia BL- 5CA will be used in this design because of its weight (20 g), with a dimension of 53 mm∗33 mm∗5 mm, a capacity of 1100 mAh, an output power of 4 Wh, and a voltage of 3.7 V.
iv. WearROBOT Battery life: The battery determines how long it can last. This is done by considering the battery capacity, energy absorbed by the reflecting material, and the energy absorbed by the sensor.
v. Environment: WearROBOT functions at a temperature of 18 to 70°C. It should function reliably for about two years on continuous operation. This system should be able to adapt to different environmental conditions.

An infrared sensor, audio system, earpiece, vibrator, buzzer, and secure digital (SD) card (SSD-card) were used in the hardware design as proof of concept. These are built around the PIC controller. The SSD card is interfaced with the PIC- chip leveraging the serial peripheral Interface (SPI).

B. WEARROBOT SUBSYSTEM DESCRIPTION

- Narrowband Infrared Sensor: Infrared receivers used in context is the photodiode. Some important specifications of infrared receivers are photosensitivity, detectivity, and noise equivalent power. Active infrared sensors comprise an infrared source and an infrared detector. The sensor consists of IR LED, and IR Photodiode (i.e., Photo–Coupler). The transmitter and the receiver were positioned at a certain angle for seamless object detection. The sensor directivity angle is +/- 45 degrees.
- SSD-Card: Micro SD card series are non-volatile, hence, external power is required to retain the stored information while running on 2.7 to 3.6 volts.
- Audio Unit: The visually impaired uses it to communicate with the outside world.
- The vibrator module is the electric motor used in daily life. This is used as a haptic technology which is applied in the tactile framework for the visually impaired to sense or touch. This is done through force application, vibration, or motions to the VI. This manual activation alerts the visually impaired to give attention to the ingress signals. For instance, the cell phone vibrating mode. Haptic adaptive technology alerts the limited vision and provides feedback from surrounding environments and movements.
- Buzzer Actuator Module – It is used as an audio signaling device built from mechanical, electromechanical, or piezoelectric material It is used as alarm devices, timers, and confirmation of user input such as a mouse click or keystroke.
- PIC-Microcontroller Unit is interfaced with the memory card. It enables the chip to select a pin on the memory card. It also ensures the appropriate clock rate for communication between it and the memory card by sending 400 kb/s to the clock pin (i.e., the serial clock pin of the memory card). The provision of communication to the memory card is done by sending appropriate serial data to the memory card. The memory card sends feedback to the PIC-chip by sending the digital equivalent of the pre-recorded voice the visually impaired should hear. The controller then takes this pre-recorded voice to the push-pull amplifier which is connected to the speaker. The push-pull amplifier has an inherent feature of converting streams of ones and zeros to their analog equivalent.

C. DETERMINATION OF SURFACE PROPERTIES

In designing the device, so many factors were considered among which are the surface properties. The surface properties suggested the best angle to be considered, the energy consumed, the battery life, the distance to the object, and the intensity of the infrared ray. These factors are of utmost importance in designing and fabricating the device for accurate detection. For the comparison of these factors and simulations, the following assumptions were made for the following reasons listed below:

- The distance to the object was kept constant to ascertain the intensity, distance traveled, and energy consumed at different distances (i.e., 5 cm, 50 cm, 0.8 m, 1 m, 3 m, 5 m, and 10 m). This aid to determine the property of the sensor considered. It reveals at what point or distance will the sensor start fading; and how the angles can boost the distance traveled.
- The energy consumed was kept constant to ascertain the distance to the object at different angles for different energy consumed. This also aids to determine the battery life of the sensor. The battery life is dependent on the energy absorbed or consumed by the device.

The different surface properties and the effect of intensity on both angle and distance to the object are studied. Appendix II shows the physical design and the interconnection of the various blocks. WearROBOT controller captures the detected signals and transmits the feedback via a buffer to a sound-buzzer, vibrator, and the audio-speaker via a high pull-up. The sound transducer, and the controller talk with the secure digital card. The chip select (CS) control achieves this function and then transmits serial data to the memory

TABLE 2. GPY0A02YK0F sensor specification.

Sensor	Sharp GP2Y0A02YK0F
Range	0.2-1.5 m
Voltage Supply (Vcc)	4.5-5.5 V
Current Consumption	33 mA
Operating temperature	-10°C to 60°C
Resolution	1 cm
Beamwidth	100
Weight	4.8 g

card using the serial data port. After sending the data, the memory card activates the controller using its serial data output port. The controller then pushes the prerecorded voice to the push-pull amplifier while disabling the CS. Recall that an infrared sensor is a transducer device that detects a physical property and responds to events. It is possible to have a physical quantity measurable by different sensors but the question about selecting the appropriate sensor has to do with the following characteristics of the sensor:

- Sensitivity: minimum physical parameter input that will create detectable output change.
- Accuracy: how close is the actual/expected value to the value measured by a sensor?

An electronic sensor for measuring a variable must be readily available, portable, selective, sensitive, accurate, reliable, durable, and at a low cost. When a sensor fails to satisfy any of the above characteristics, then the variable or quantity to be measured cannot be incorporated into the system and thus the integrity of the system is undermined.

In this article, four (4) sharp long-range infrared GP2Y0A02YK0F sensors were placed at the right, left, front and rear sides of the device as shown in Figure 3. The sensors have a range of 0.2 m to 1.5 m; a consumption current of 33 mA. The acceptable input voltage ranges from 4.5 to 5.5 V.

As shown in Figure 3, the battery life of the sensor determines the longevity of the WearROBOT device [65]. With the battery capacity and the energy absorbed by the nodes, this is determined. Energy is equally absorbed by the microprocessor due to the active state of the device. A simple DC supply explores the battery energy, But the 12 V power supply is controlled up to 5 V TTL 7805-voltage chip regulator. This regulated output is used to power the microcontroller via a user toggle switch. Filtering is completed using capacitors C_1 and C_2. This prevents unnecessary voltages that have spikes. A 100 μF capacitor drops the voltage transients on the regulator input while enhancing the voltage output stability. The four-IR sensors were tested with a secure digital card and the digital oscillator circuit. The oscilloscope confirmed the status of the SD card and the corresponding waveforms.

Table 2 shows the specification of a sharp GP2Y0A02YK0F sensor.

- Secure Digital (SD) card: This communicates with the controller via the Serial Peripheral Interface (SPI). The SD cards are universal low-cost, the high-speed card with data storage media.

The microcontroller communicates with the SD card by sending data serially to the card. This is done by activating the chip select (CS) by making it LOW. Once is LOW, data can be exchanged between the SD card and the controller. The IR transfer rate is usually 400 kb/s.

- Distance measurement: Infrared (IR) sensors were used as proximity sensors in obstacle avoidance.
- Determination of the surface property of the obstacle detection as well as the orientation angle of the surface with the IR sensor is investigated including the distance to the object.
- Battery capacity, size, and weight: BL-5CA Nokia battery model is employed.
- Battery Life Sensing- This is implemented to support the sensors optimally.
- The battery capacity (Bc) and the energy absorbed by the sensor were benchmarked. The microprocessor monitors the battery life of the device as it absorbs constant energy aside from the energy consumed because of the device's active state as shown in Figure 3.

Contextually, the term ''angle'' as mentioned in this article refers to the angular positional displacement from the patient or visually impaired relative to the obstacle detected. The wearable robot can be titled to any angle to detect obstacles while noting the distance from the object and the intensity of surface impact. For experimental convenience, four infrared sensors were wired together to increase surface impact and sensitivity through posterior probabilities. As shown in Figure 4, there are Wear-ROBOT **S1**, **S2**, **S3**, and **S4**triggered continuously by an astable multivibrator (N555 timer). With the LMCG algorithm, the controller responds immediately to an object that is sensed while activating a buzzer, vibrator, etc. Figure 3 shows the simplified wired schematics.

The link budget considerations for the IoT-enabled sensor node and LP-WANs are given by Shannon–Hartley theorem [62] in (15).

$$\frac{E_b}{N} = \frac{\varepsilon}{Cp}\left[2^{\frac{Cp}{g}} - 1\right] = \frac{2^n - 1}{n} \tag{15}$$

where

$Cp =$ *capcity(bits/s)*
$\varepsilon =$ *bandwidth*
$n =$ *Spectral efficiency (bit/s/Hz)*
$\frac{1}{C_p} =$ *Bit duration*
$E_b = \left(\frac{S}{Cp}\right)$ *in Joule*
$N.\varepsilon =$ *Total noise power (watts)*

As shown in Figure 5, the WearROBOT signals are fully decapsulated at the receiver node. Hence, the threshold energy detected is based on the node receiver sensitivity (σ) as highlighted in (16) [63].

$$\sigma = \frac{E_b}{N} + 10.\log_{10} Cp + (\vartheta - 174\,dBm)$$

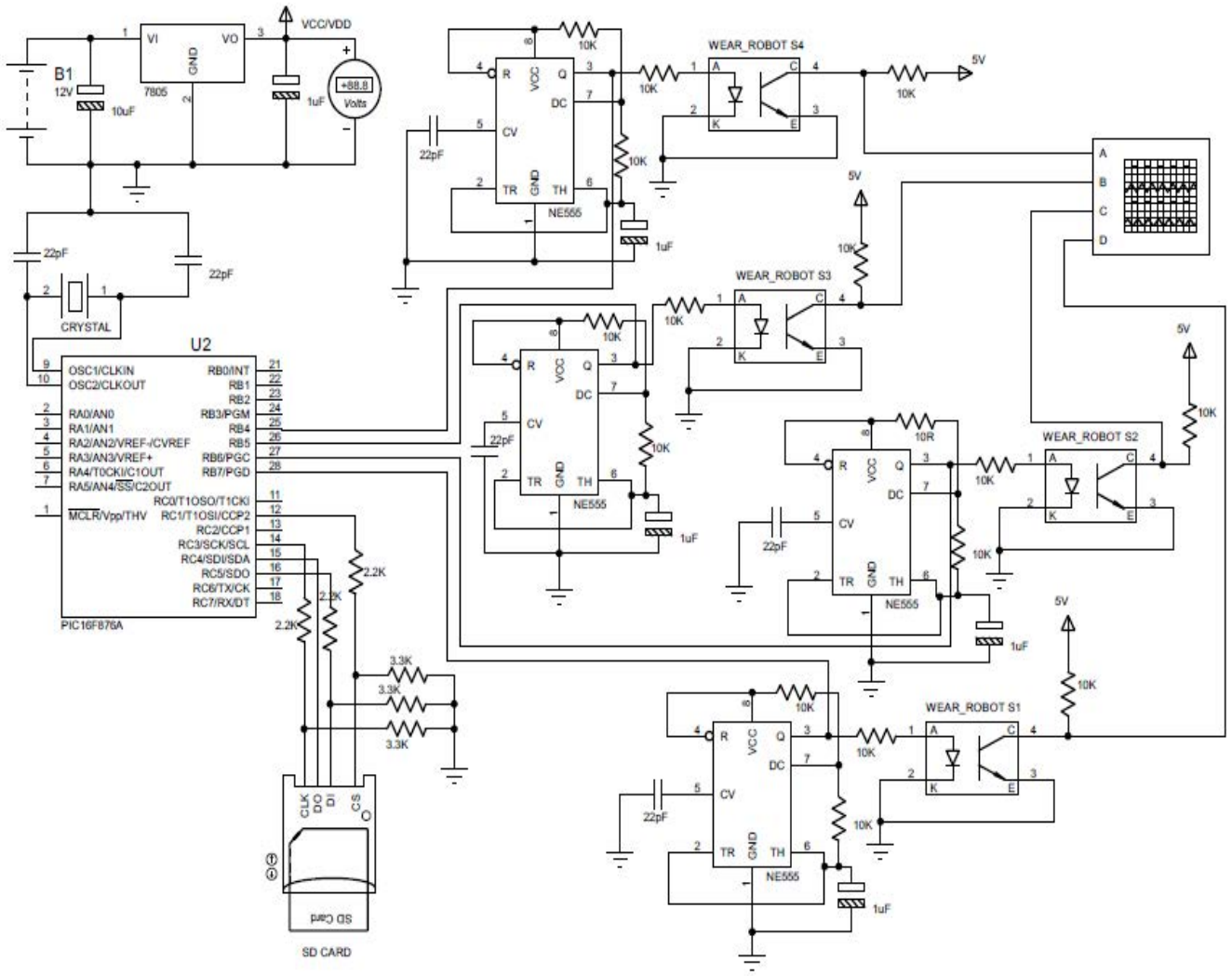

FIGURE 3. **WearROBOT Link capacity utilization schematics (Proof of concept).**

$$\vartheta = Noise\ figure\ (2-6\,dB) \tag{16}$$

The potentially available IR throughput per coverage unit is given by (17).

$$R(\lambda,\theta) = \lambda.\log_2(1+\theta)\,\mathrm{P_r}(\mathrm{SNR} \geq \theta \tag{17}$$

where

$\lambda =$ *IR* optional Fog or gateway density
$P_r(.) =$ *IR probability operator*
$\theta =$ *IR SNR threshold*
$R =$ *IR Throughput* ($bps/Hz/Km^2$)

In a scenario of cascaded cluster gateways connecting the IR sensor nodes, the area spectral efficiency (ASE) is given by (18) [64].

$$\psi A(\lambda) = \lambda.\tau\left[\log_2(1+SNR)\right], \quad SNR \geq \theta \tag{18}$$

This (18) gives the bit rate adaptation based on the SNR rather than a signal outage. Figure 5 shows prototype system derived from similar efforts [65]. The summarized WearROBOT is decomposed into a PIC controller, input sensors (ultrasonic sensor, accelerometer, voice synthesizer), and output actuators (sound buzzer, and vibrator). These are labeled as follows. **A**: Voice recognition module (VRM), **B**: GSM-IoT Module (GIM), **C**: Buzzer translation, **D**: Microphone tab, **E**: BIOS chipset, **F**: Primary breadboard, **G:** rear GIM, H: PIC controller, **I**: IR sensor Antenna, **J**: Accelerator, **K**: Ultrasonic sensor, L: Motion vibrator. Figure 4 shows the test rig for the WearROBOT node.

Using the setup in Figure 5, optimal sensor placement positions for detection of rear-side, front-side, right-side, and left-side obstacles were calibrated. The design of a miniaturized wearable obstacle detector was derived in Figure 5. Also, the work integrates a scalable transducer feedback routine into the wearable obstacle detector system.

In Section VI, the performance evaluation via the simulation studies is presented. Energy consumption, energy

FIGURE 4. WearROBOT simulation testbed at IEEE MSR-Lab, FUTO.

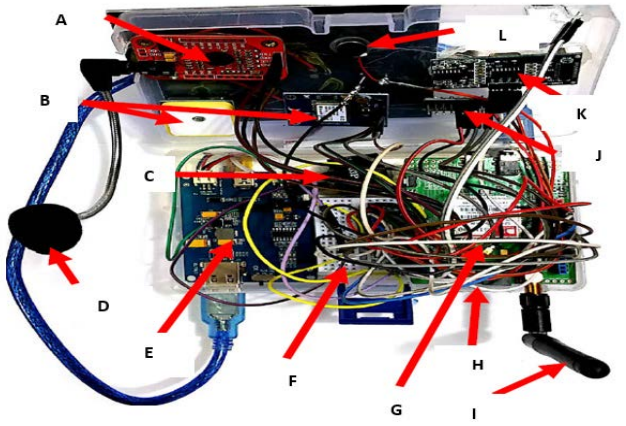

FIGURE 5. WearROBOT proof of concept reference hardware.

latency, battery life performance, and system validation of LMCG are discussed.

VI. SIMULATION ANALYSIS

In this section, over 1000 limited vision-agent community representatives were considered in the simulation training using the Protus C++ API library in Figure 4. The setup comprises 1GB GPU RAM size running on Intel Core i5 CPU, and 8 GB RAM. IEEE MSR-Lab in the SEET complex, at the Federal University of Technology Owerri, Nigeria was used for the investigations. Also, the proof-of-concept simulation setup for numerical analysis was configured in Figure 4. A comparison of the effect of angle positions of the sensor on the device is evaluated considering β. The simulation was done to compare the effect of node wearable-node angle to intensity, distance traveled, and energy absorbed at different distances to the object while considering various angles.

For the WearROBOT LMCG network, the localization size of the network was considered in the selected GPU memory employed during the trials. Figure 4 has Riverbed 17.5 sensor libraries which were configured through trace files using the radio energy dissipation model and simulation parameters [34]. In this paper, Fresnel clearance, path loss, coverage, and link budget have been fully considered [34].

TABLE 3. Intensity of infra-ray, distance traveled, and energy absorbed at 5 cm.

Angle	Distance (cm)	Intensity W/m^2	Energy Absorbed (J)	Distance traveled (m)
20^0	5	18	6000	0.055
30^0	5	16	4000	0.06
40^0	5	12	2500	0.07
45^0	5	5	1900	0.08

TABLE 4. Intensity of infra-ray, distance traveled, and energy absorbed at 50 cm.

Angle	Distance (cm)	Intensity W/m^2	Energy Absorbed (J)	Distance traveled (m)
20^0	50	1.8	6	0.0525
30^0	50	1.5	4.5	0.05
40^0	50	1.2	3	0.65
45^0	50	1.1	2	0.7

The simulation analysis involves obstacle detection using various distances with angular displacements. Figure 6a shows that at 5 cm (distance) with an angle of 45^0, the intensity of object detection is 11 W/m^2. This happens at the traveled distance of 0.08 m in Figure 6b. In this case, the energy absorbed is 18 kJ as shown in Figure 6c. This can be shown in Table 3 depicting different angles with their corresponding intensity, energy absorbed, and distance traveled.

Figure 7 shows that at 50 cm with a wearable angle of 45^0, the intensity is 1.1 W/m^2. Also, the energy absorbed is 2 J and the distance traveled is 0.7 m. Table 4 shows different angles with their corresponding intensity, energy absorbed, and distance traveled.

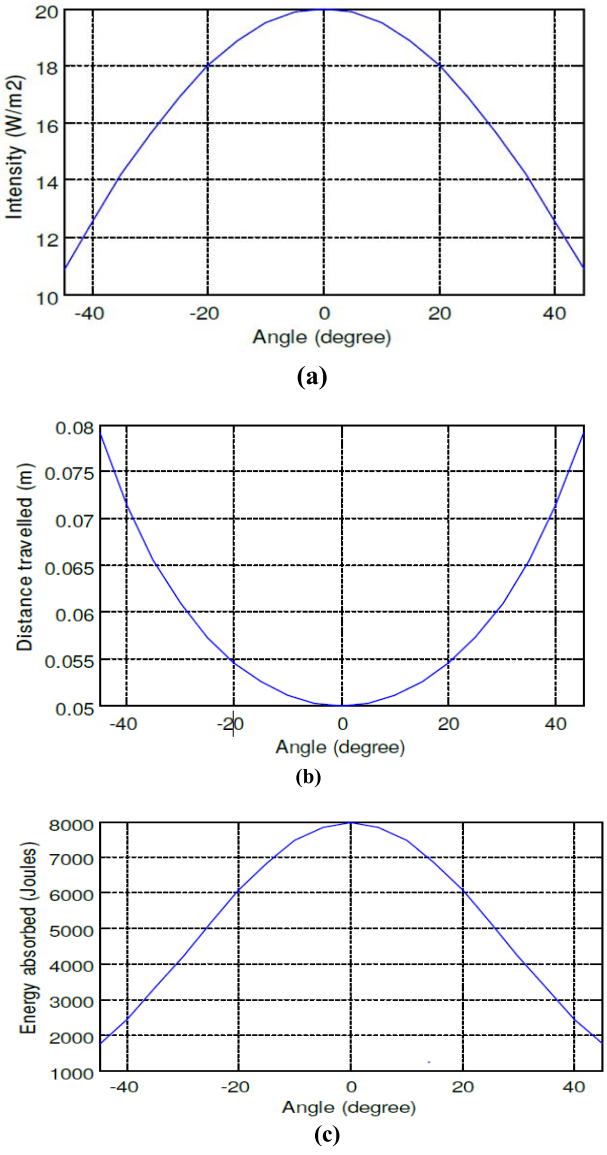

FIGURE 6. Illustration of the intensity of the infrared ray, distance traveled, and energy absorbed at 5 cm. (a) Experimental linear intensity response (b) distance traveled response (c) Energy absorbed response.

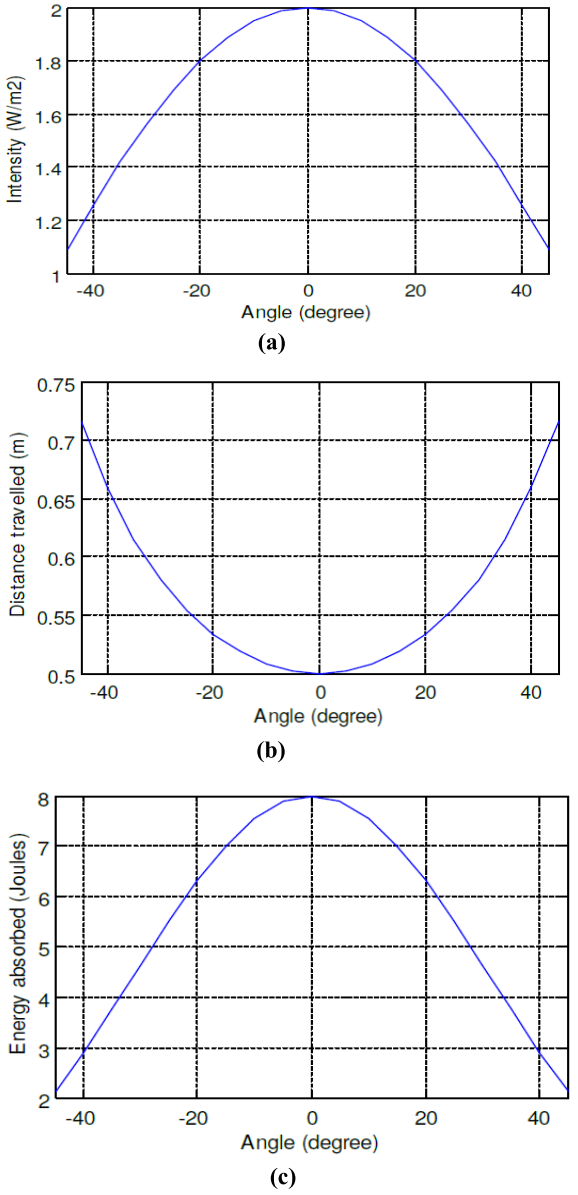

FIGURE 7. (a-c) Illustration of Intensity of the Infrared Ray, distance Travelled, and energy absorbed at 50 cm.

TABLE 5. The intensity of infra-ray, distance traveled, and energy absorbed at 5 cm.

Angle	Distance (cm)	Intensity W/m²	Energy Absorbed (J)	Distance traveled (m)
20^0	0.8	1.1	1.5	0.85
30^0	0.8	0.9	1	0.9
40^0	0.8	0.75	0.75	1.05
45^0	0.8	0.7	0.5	1.15

TABLE 6. The intensity of infra-ray, distance traveled, and energy absorbed at 1 m.

Angle	Distance (cm)	Intensity W/m²	Energy Absorbed (J)	Distance traveled (m)
20^0	1	0.9	0.8	0.05
30^0	1	0.8	0.6	1.15
40^0	1	0.63	0.4	1.3
45^0	1	0.55	0.3	1.4

Fig. 8 shows that at 0.8 m with a wearable angle of 45^0, the intensity is 0.7 W/m^2. The energy absorbed is 0.5 J and the distance traveled is 1.15 m. Table 5 shows the different angles with their corresponding intensity, energy absorbed, and distance traveled.

Figure 9, shows that at 1m with an angle of 45^0, the intensity is 0.55 W/m^2; energy absorbed is 0.3 J, and the distance traveled is 1.4 m. Table 6 depicts the different angles with their corresponding intensity, energy absorbed, and distance traveled.

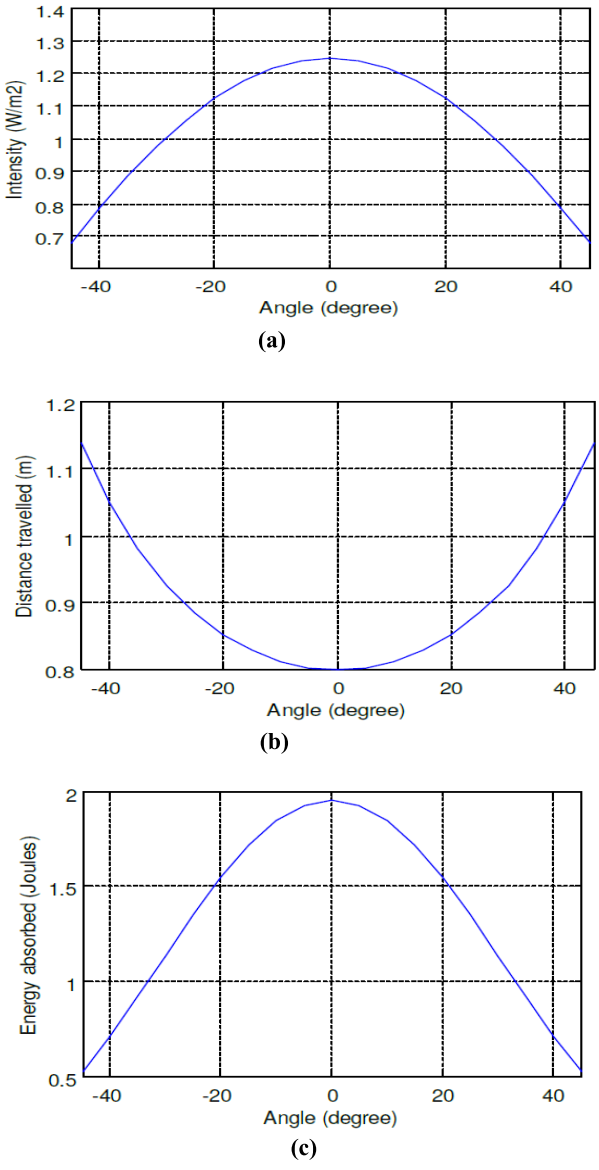

FIGURE 8. Illustration of the intensity of the infrared ray, distance traveled, and energy absorbed at 0.8 cm. (a) Experimental linear intensity response (b) distance traveled response (c) Energy absorbed response.

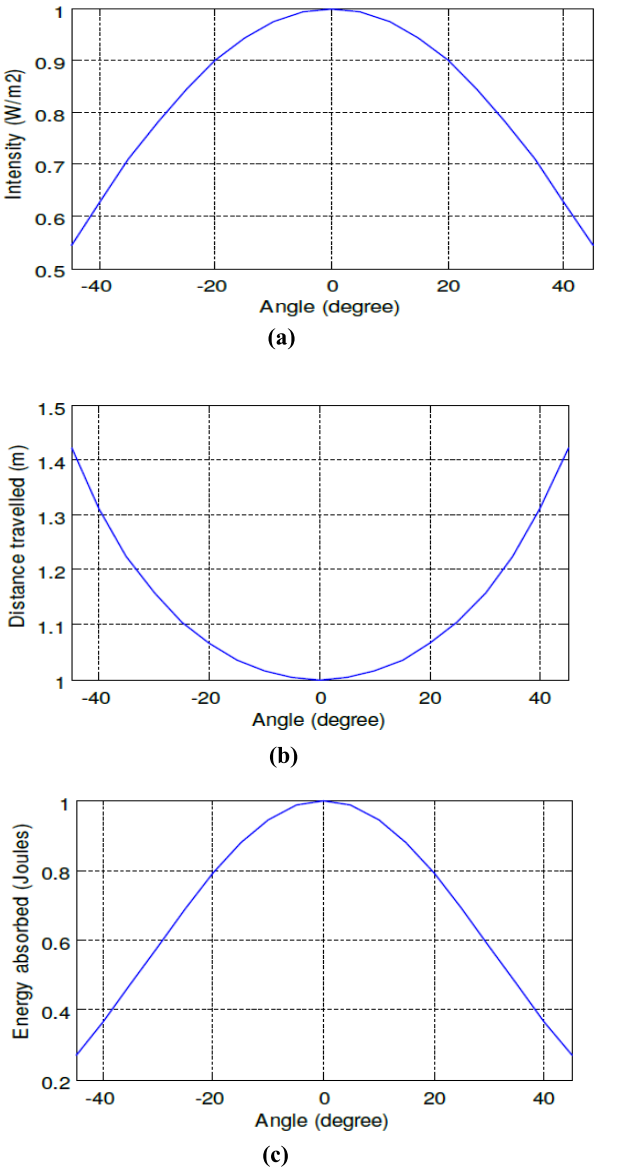

FIGURE 9. (a-c) Intensity of the infrared ray, distance traveled, and energy absorbed at 1 m.

TABLE 7. The intensity of infra-ray, distance traveled, and energy absorbed at 3 m.

Angle	Distance (cm)	Intensity W/m^2	Energy Absorbed (J)	Distance traveled (m)
20^0	3	0.3	0.03	3.25
30^0	3	0.25	0.02	3.5
40^0	3	0.22	0.0125	4
45^0	3	0.04	0.01	4.25

TABLE 8. Intensity of infra-ray, distance traveled, and energy absorbed at 5 m.

Angle	Distance (cm)	Intensity W/m^2	Energy Absorbed (J)	Distance traveled (m)
20^0	5	0.18	0.006	5.03
30^0	5	0.15	0.005	5m
40^0	5	0.12	0.003	6.5m
45^0	5	0.10	0.002	7m

Figure 10 shows that at 3m with a wearable angle of 45^0, the intensity is 0.04 W/m^2. The energy absorbed is 0.1 J and the distance traveled is 4.25 m. Table 7 shows the different wearable angles with their corresponding intensity, energy absorbed, and distance traveled.

Figure 11, shows that at 5 m with an angle of 45^0, the intensity is 0.10 W/m^2. The energy absorbed is 0.002 J and the distance traveled is 7 m. Table 8 shows the different angles with their corresponding intensity, energy absorbed, and distance traveled.

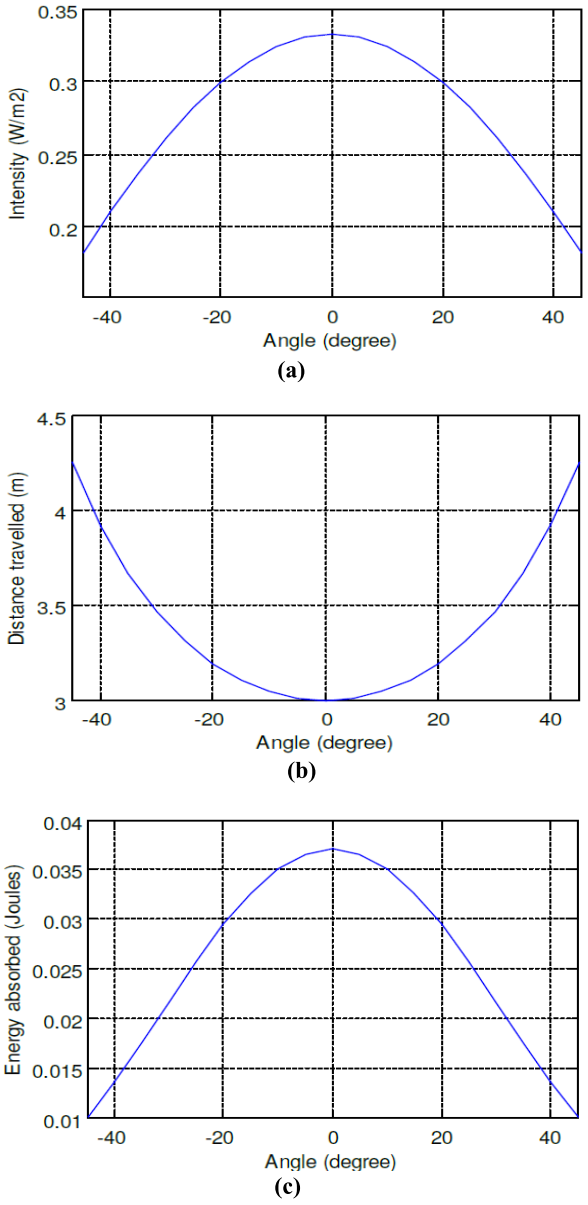

FIGURE 10. (a-c) Intensity of the infrared ray, distance traveled, and energy absorbed at 3 m.

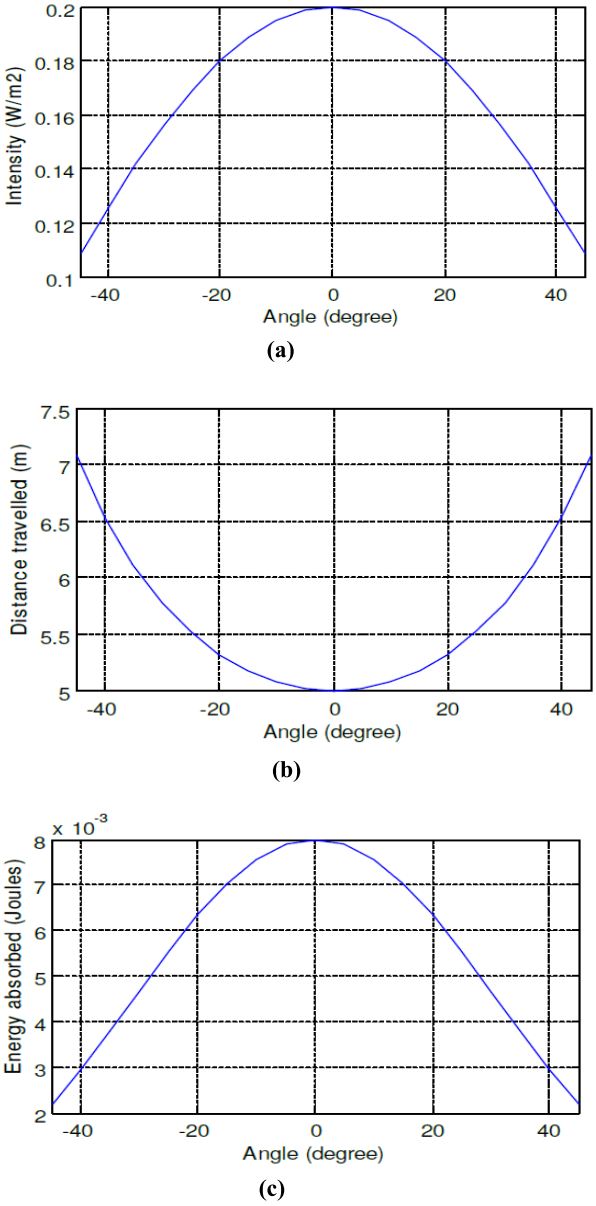

FIGURE 11. (a-c) Intensity of the infrared ray, distance traveled, and energy absorbed at 5 m.

TABLE 9. Intensity of infra-ray, distance traveled, and energy absorbed at 10 m.

Angle	Distance (cm)	Intensity W/m^2	Energy Absorbed (J)	Distance traveled (m)
20^0	10	0.09	0.0008	10.8
30^0	10	0.075	0.0005	11.5
40^0	10	0.06	0.0004	13
45^0	10	0.055	0.0003	14

Figure 12 shows that at 10m with an angle of 45^0, the intensity is 0.10 W/m^2, energy absorbed is 0.002 J and the distance traveled is 7 m. Table 9 shows the different angles with their corresponding intensity, energy absorbed, and distance traveled.

Figure 13 shows the relationship or the effect of the wearable angle on distance using LMCG. This is achieved by keeping the energy absorbed constant while comparing the different energy absorbed. The result shows that there was a progressive decrease in distance as the absorbed energy increased. It gives a guideline for the wearable angles and different distances to consider in the device design. The result suggests an increase in the angle if a lower distance is desired for the energy absorbed. Comparison of the battery life was considered based on the distance an object is placed. It is seen that the battery life increases as the distance increases with an increased wearable angular displacement. An increase in wearable angle positioning increases the

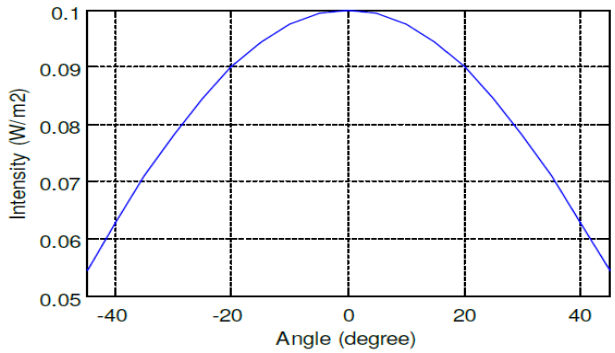

(a)

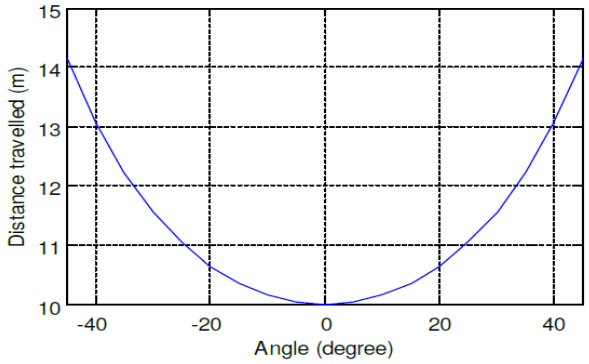

(b)

FIGURE 12. (a-b) Intensity of the infrared ray, distance traveled, and energy absorbed at 10 m.

TABLE 10. Battery life at distance travelled with wearable sensor angular displacement.

Distance (m)	Battery @A_i	Battery@A_1	Battery@A_2	Battery@A_3
4.41E-01	3.83631714	3.79E+00	3.72E+00	1.83E+00
7.16E-01	9.97E+00	9.13E+00	1.08E+01	5.06E+00
9.46E-01	1.71E+01	1.49E+01	1.90E+01	8.69E+00
1.20E+00	2.76E+01	2.16E+01	2.65E+01	1.41E+01
1.41E+00	3.84E+01	2.98E+01	3.82E+01	2.10E+01
1.63E+00	5.14E+01	3.85E+01	5.30E+01	2.94E+01
1.81E+00	6.45E+01	4.88E+01	6.75E+01	3.93E+01
2.00E+00	7.80E+01	6.12E+01	7.92E+01	5.24E+01
2.21E+00	9.26E+01	7.17E+01	9.28E+01	6.04E+01

NB: $A_0 = 5^0, A_1 = 15^0, A_2 = 35^0, A_3 = 45^0$

battery life of the wearable sensor device due to displacement kinematics. Table 10 gave the summary of the evaluation study while justifying the proposed scheme for WearROBOT. Figure 14 shows the WearROBOT battery optimization with LMCG. The comparison between an unoptimized wearable node and a reference node is depicted in the plot. About 63% of the battery life results from wearable node optimization while the unoptimized node had 31.58% battery life in Figure 14. Also, it is observed that a typical wearable node without LMCG has 5.42% battery life.

Figure 15 shows the number of batteries against the weight of the device. It can the seen from the graph that the number of batteries affects the device's weight. The result further shows that the battery weight 120 grams since three batteries were used.

Figure 16 shows the battery capacity against the weight of the device. It can the seen from the graph that the battery capacity affects the weight of the device. It was observed that the battery capacity is 11.1 V while the weight of the device is 121 grams.

VII. PERFORMANCE VALIDATIONS

The WearROBOT validation is presented for the LP Multi-commodity graph (LMCG-IoT). The LMCG robotic scheme/mode with narrowband IR IoT (LMCG -NB-IoT) was compared with Bluetooth Low-Energy (BLE-IoT) and Low Power WAN (LP-WAN) schemes. As shown in Figure 17, the amount of energy used for each operation performed by the communicating wearable sensor under the LMCG is discussed. Energy consumed is investigated by considering the measurement distances of the nodes. Previously, the controller sensor and RF units are the key energy consumers. The sensor node's transceiver component uses most of its energy. The sensor node will need to retransmit the proposed LMCG -NB-IoT frame in this situation.

According to [66], the proposed LMCG -NB-IoT standard can transmit a packet signal up to eight times if the downlink frame is corrupted. Considering the sensor tasks viz-a-vis distance from the nodes, energy consumption was observed. In Figure 17, as the wearable robot moves away from the node-obstacle, LMCG NB-IoT drops energy significantly. The LP-WAN, BLW-IoT and proposed LMCG-NB-IoT offered 51.28%, 33.33%, and 15.39% respectively. This energy sensitivity analysis has implications as regards the maximum coverage distance needed for full connectivity. The proposed LMCG-NB-IoT has the least energy drain for the selected distance coverage.

In terms of energy latency in Figure 18, this deals with latency experienced by the transceiver nodes due to space diversity constraints. The payload size, travel time, and external factors like temperature all have an impact on the active device life across all technologies. Extreme weather conditions have been found to severely shorten the active IoT device life within the LP-WAN in addition to the imposed load. The LP-WAN, BLW-IoT, and the proposed LMCG-NB-IoT had 65.63%, 31.25%, and 3.12% respectively. The latency profile of the proposed LMCG-NB-IoT makes WearROBOT highly sensitive and responds quickly to external actuation.

In Figure 19, LoRa-WAN, LP-WAN, BLE, and the proposed LMCG-NB-IoT had battery life profiles of 80%, 96.6%, 100%, and 50% respectively. Also, from Figure 19, the transmitted signal is received and acknowledged upon impacting an obstacle. A demodulation process at the receiver sink is used to verify success in transmission. In this case, more energy would have been consumed. The energy

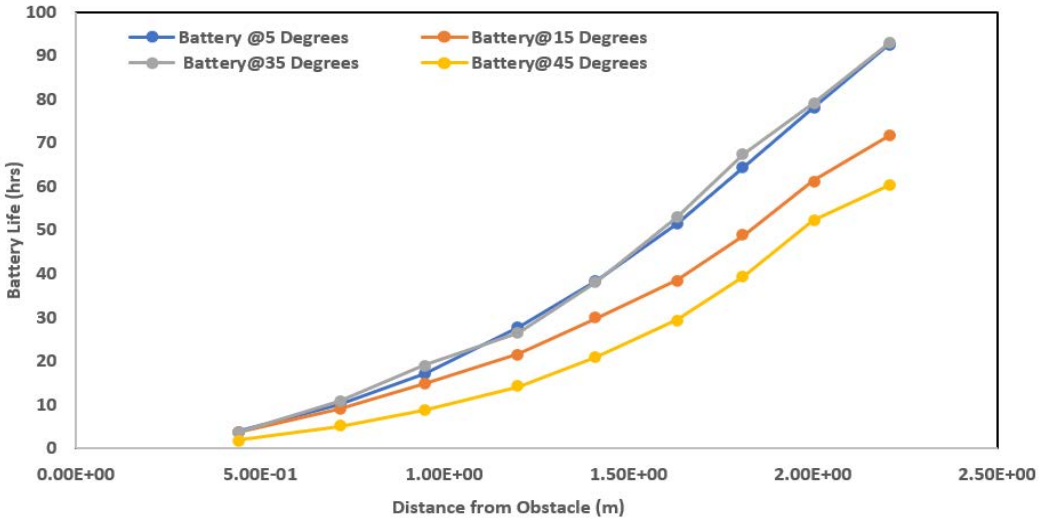

FIGURE 13. Comparison of battery life vs distance at various angles.

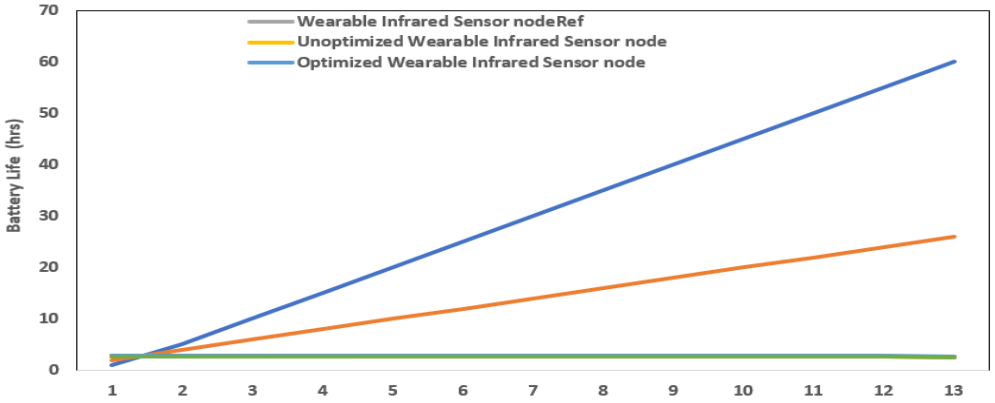

FIGURE 14. Comparison of battery life with WearRobot Node optimization.

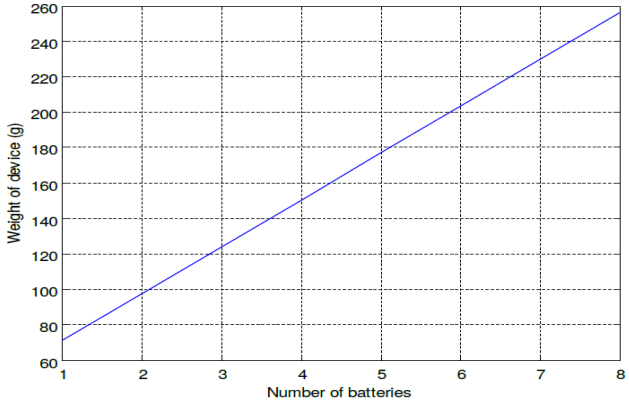

FIGURE 15. Weight against several batteries.

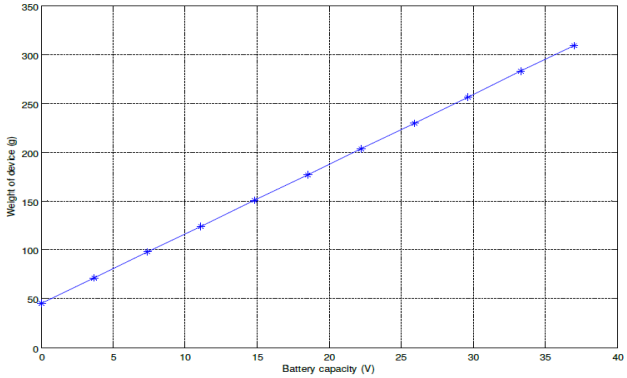

FIGURE 16. Weight concerning battery capacity.

dissipated by the nodes is smaller in the proposed LMCG -NB-IoT compared to the other schemes as shown in Figure 19.

In this case, the IR communication node sends data to the controller upon detecting an obstacle. Recall that the BLE mode operates from 2.402 GHz to 2.48 GHz and stays asleep in between connections. Since it only communicates for a few seconds at connection, switching off between transmissions allows BLE nodes to communicate effectively at fractional power. The indeterminate state in Table 11 explains close to 100% power savings in bidirectional communication while

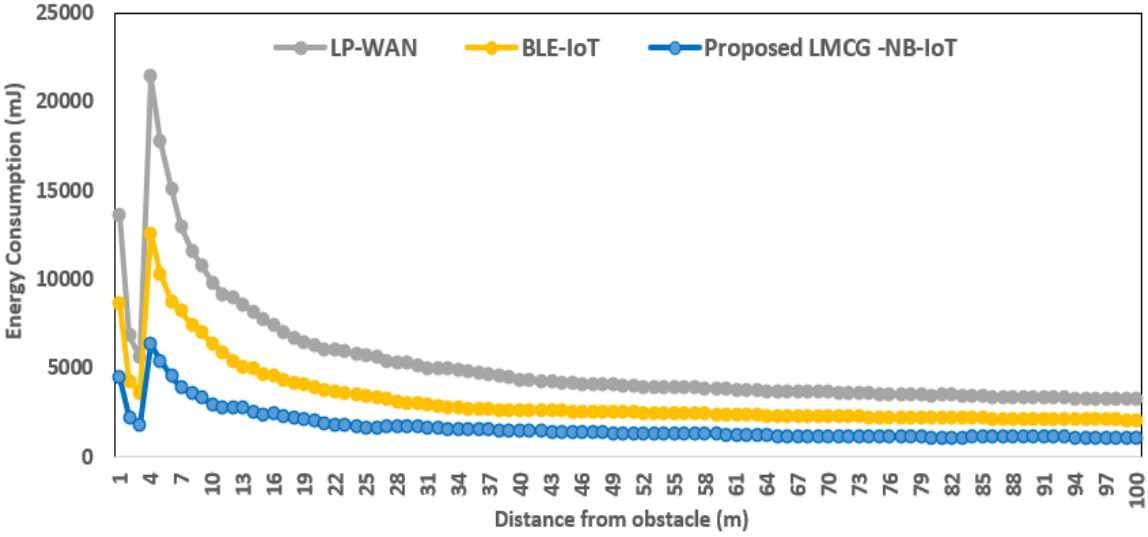

FIGURE 17. Impact of sensor distance placement on the energy consumption profile.

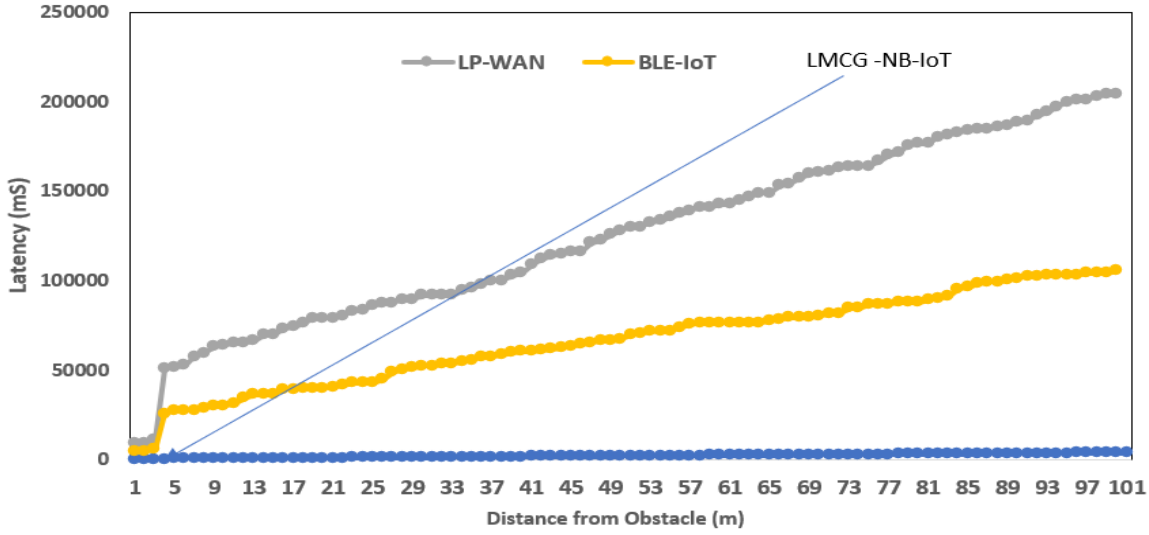

FIGURE 18. Impact of sensor distance placement on energy latency profile.

offering data transfer at 125 kBs to 2 MBs. It does so with a latency of about 6ms consuming between 0.01 and 0.5 W. Hence, the indeterminate status implies that the battery life will be longer as it uses 100 times less power under small workloads.

Fig. 20 shows the various angular orientations of the WearROBOT vis $A_0 = 5^0, A_1 = 15^0, A_2 = 35^0, A_3 = 45^0\ A_4 = 65^0\ A_5 = 75^0$ At each angular displacement, the intensity of impact on the surface is shown. An increase in angular orientation leads to corresponding surface intensity impact. This makes the wearable entity respond more intuitively to sudden impacts. To validate the proposed work, quality of user experience (QoUE), computational workload (CWL), and average latency profile (ALP) were employed

TABLE 11. Validation results summary (case 1).

Target Schemes	Energy Consumption (mJ)	Latency (msec)	Battery Life(h)
LP-WAN Mode	51.28%	65.63%	96.6%
BLE_Mode	33.33%	31.25%	Indeterminate (100%)
Proposed LMCG_Mode	15.39%	3.12%	50.00%

in the proposed LMCG, MMSN, and GHMMs respectively. In terms of QoUE in Figure 21, the work yielded 41.18%, 23.53%, and 35.29% respectively. This implies that the patient can use the device comfortably. In terms of CWL in

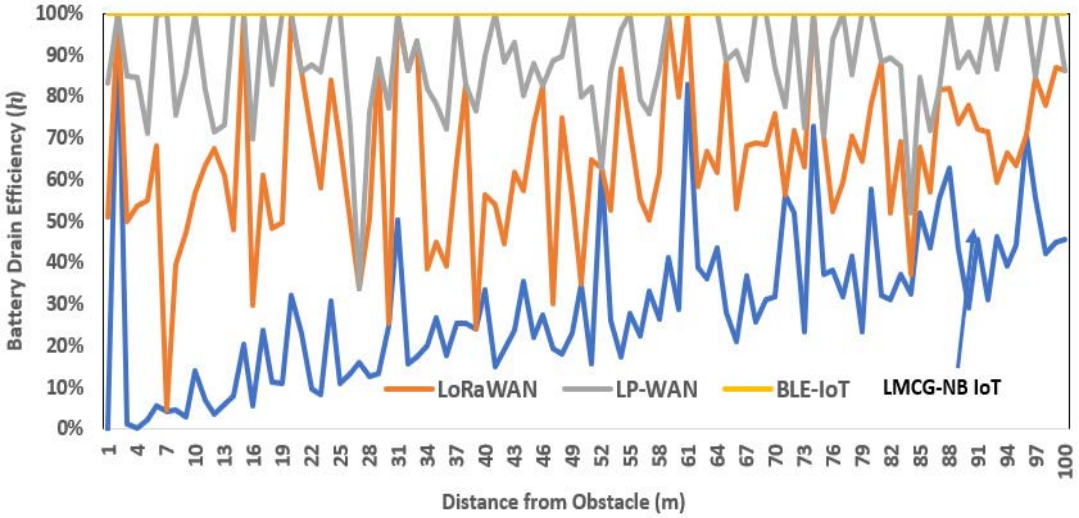

FIGURE 19. Impact of sensor distance detection on Battery life profile.

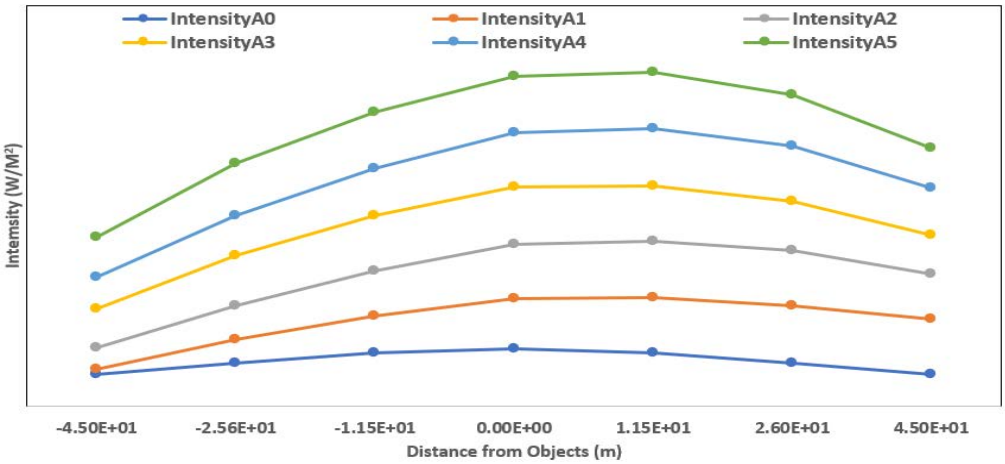

FIGURE 20. Impact of sensor distance detection on battery life profile.

TABLE 12. Validation results summary (case 2).

Target Schemes	QoUE	CWL	*ALP*
Proposed LMCG	41.18%	51.14%	32.97%
MMSN	23.53%	28.41%	33.59%
GHMMs	35.29%	20.45%	33.44%

Figure 22, this gave 51.14%, 28.41%, and 20.45% respectively. Finally, the ALP in Figure 23 gave 32.97%, 33.59%, and 33.44% respectively.

In summary, Figure 22 shows very high computational workload utilization for the WearROBOT LMCG. The active clocking of the CPU, battery, power management routine, vibration, audio, and displays offers a huge workload depicted in plot. By including other sensors such as gyroscopes, accelerometers, etc, much signal processing will be required. Ultimately, after the processing, a convergence behavior was observed showing good performance. Hence, an optimal processing computation will support extensive battery life management functionality. Figure 23 shows the latency response of the WearROBOT LMCG. The lower latency behavior has been verified in the LAB testbed even when tested with external Universal Serial Bus (USB), universal asynchronous receiver transmitter (UART), synchronous serial communication interface (SPI), and Inter-Integrated Circuit (I2C) interfaces. The lower latency allows for measurement of impedance (such as galvanic skin response, GSR), measurement of voltage (e.g., right-hand drive ECG monitoring), measurement of current for photoplethysmography LED function, sensing of pulse rates, and measurement of oxygen saturation level SPO2. With the lower latency profile, accuracy optimization and speed adaption will be very useful in applications such as fitness-wearable pulse rate monitoring systems.

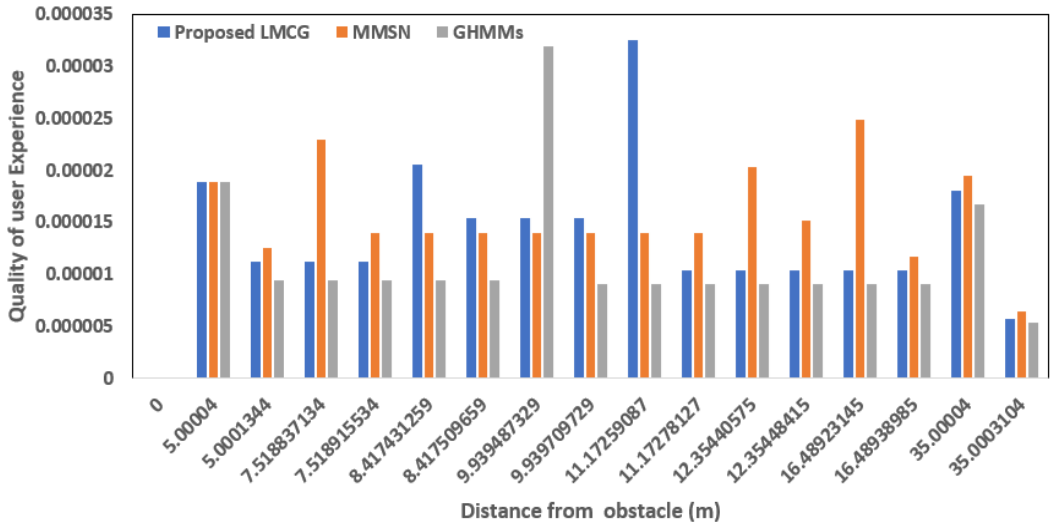

FIGURE 21. Quality of user experience metric validation.

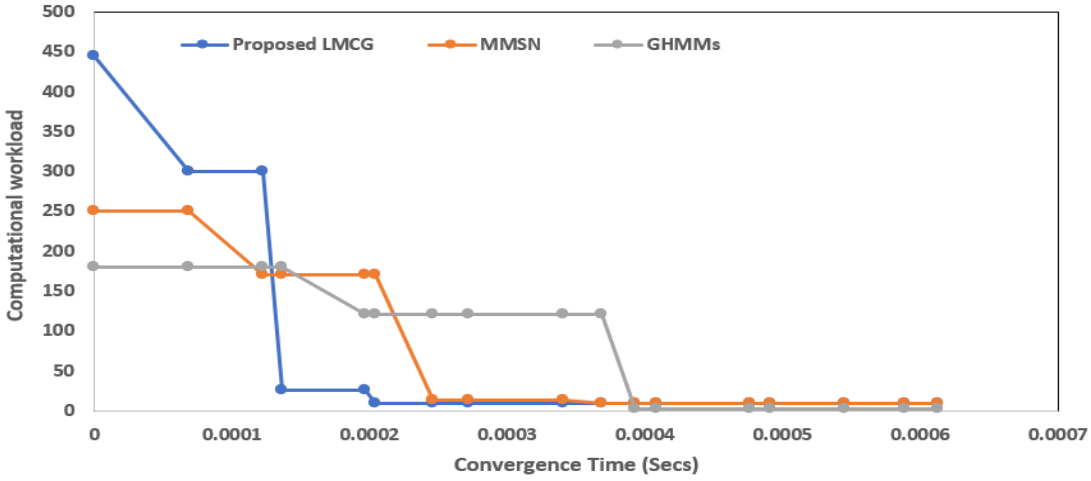

FIGURE 22. Computational workload validation.

TABLE 13. Technical feasibility comparison of AALS.

Target Schemes	ATTRIBUTES	DESIGN TYPE	QoUE	CWL	*ALP*
This work (LMCG)	- Space diversity - Confidentiality - Maintainability - Trustability - Resource control	- Open Source - Hybrid Low latency system	41.18%	51.14%	32.97%
MMSN [46]	- Reliability - Integrity - Availability	-Machine Learning - Embedded Systems - Non-Open Source	23.53%	28.41%	33.59%
GHMMs [45]	- Computational workload - Non-linear distortion	- System Identification - Data Measurement	35.29%	20.45%	33.44%

So far, this article has identified some trade-offs in terms of cost, computational workload, energy efficiency, and quality of user experience. For instance, the battery energy life preservation is at the expense of a huge computational workload estimated at 51.15% unlike other schemes with lower computational workloads such as MMSN and GHMM having 28.41% and 20.45% respectively (See Table 12).

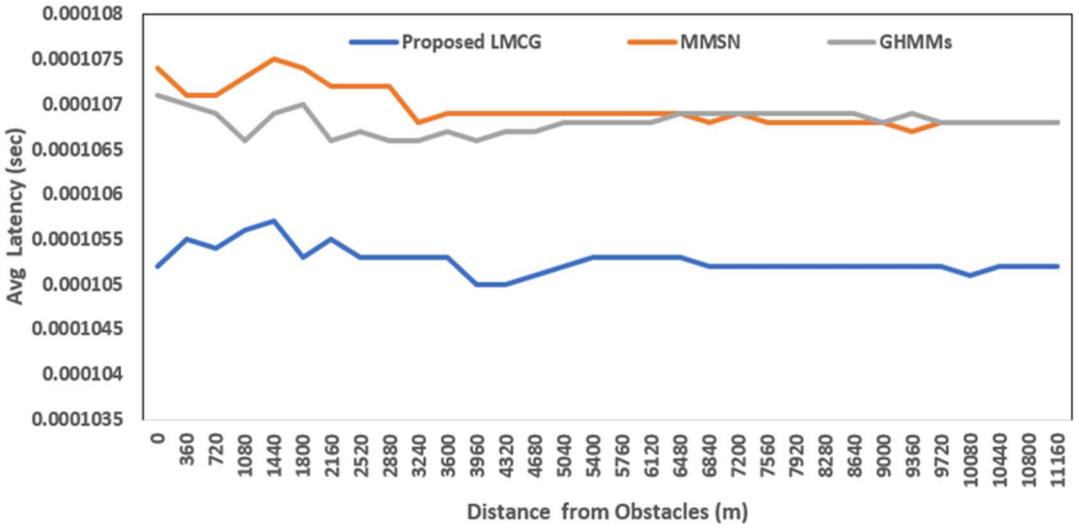

FIGURE 23. Computational workload latency validation.

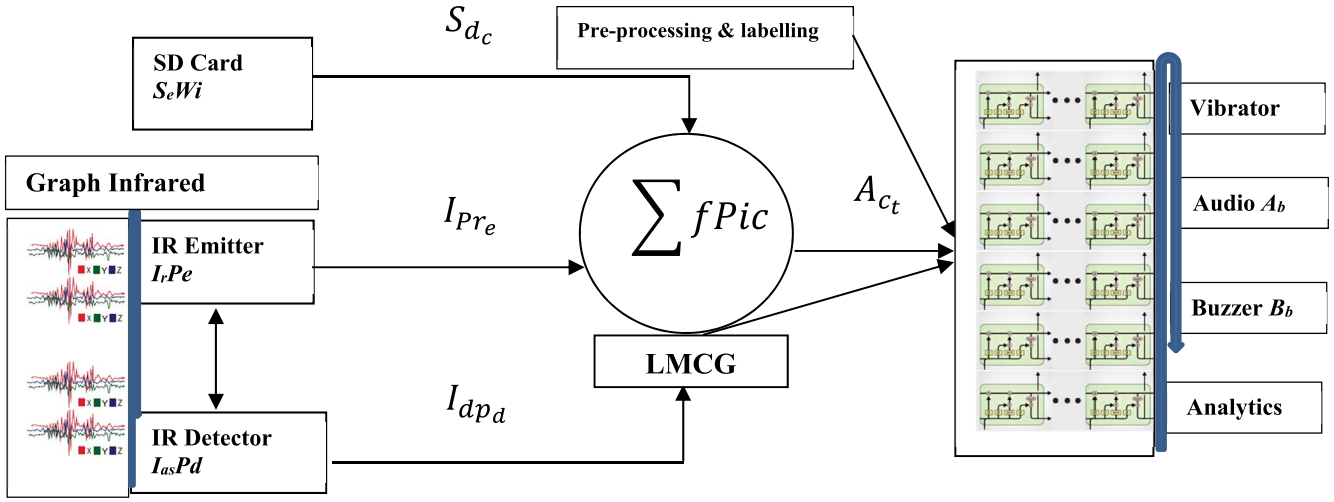

FIGURE 24. WearROBOT Flow Convergence Architecture.

Also, the introduced Quality of user experience has associated cost-overhead. The WearROBOT is a non-invasively worn-body sensor that uses LMCG to monitor obstacles as well as variants of real-time physiological attributes. The design could be well adapted for capturing body temperature, respiration/heart rate, variability, or even perfusion attribute. All these could add to the computational workload overhead.

Finally, WearROBOT data extraction and analysis will require a lightweight spike neural network to save battery life extensively. With LMCG, battery life can be enhanced but this has significant cost implications. Big data analytics is largely power-driven and may not be well suited for WearROBOT. At rest state, WearROBOT will explore machine and deep learning schemes to benchmark the efficiency of patient-driven data acquisition. However, LMCG cannot solve the big data optimization problem. In this case, lightweight edge computing can be explored for sensor data analysis. This is preferable and less time-consuming while offering a reasonable trade-off in terms of the computational workload of the CPU.

VIII. CONCLUSION

This paper presented an Energy Conservative Wearable Obstacle Detection Robot based on the LP Multi-Commodity Graph flow technique. This relies on the concept of the Infrared shortest distance path method for obstacle detection. This was used to establish foundations for WearROBOT needed for assisted living communities and related applications. Specifically, the work investigated the proposed LP multi-commodity graph IR sensor implementation under reliable communication. The determination of the optimal sensor placement position that facilitated detection of rear-side, front-side, right-side, and left-side obstacles was realized. An embedded wearable obstacle detector using an infrared sensor was achieved. The performance characteristics of the designed system including the battery energy

conservation, life performance, reflectivity, spanning distances, and integration of an audio feedback system into the wearable obstacle detector system were accomplished. The formulation of the Infrared sensor problem function that minimizes link utilization considering traffic demand was discussed with optimality variables.

Various analysis on distances with angular positions was investigated. The system validation involving the LP Multi-Commodity graph (LMCG-IoT) modes was investigated. Narrowband IR IoT (LMCG -NB-IoT) was compared with Bluetooth Low-Energy (BLE-IoT) and Low Power WAN (LP-WAN) modes. Energy consumption, energy profile, and battery life were compared in the WearROBOT contexts. The proposed scheme converges faster than existing schemes, especially in terms of transaction energy resources. WearROBOT has energy consumption as a critical constraining factor in the IoT-based sensor implementation. Therefore, an optimized energy path algorithm for sensor nodes has been achieved.

The results show that the transmitted and received acknowledgment drains energy and this drops the sensor node lifetime. Therefore, the energy path is optimized to minimize fast drain in prolonged exposure. Under varying distances, the Angle-Intensity analysis (AIA) is measured. Optimizing narrowband IR-IoT parameters is necessary for energy consumption reduction. Hence, the work showed the real application case of the multi-commodity graph energy algorithm using sensor design architecture. In this case, the energy consumption of the sensor node as well as a lifetime can be estimated considering an acknowledgment transmission. The optimized shortest path first algorithm on Infrared wearable hardware provided sufficient insight via numerical results. Future work will include the design of a spike AI energy model for processor power management in sensor nodes via energy harvesting to maximize the sensor node lifetime.

APPENDIX I.

NOMENCLATURE

$\boldsymbol{h_d}\ (1, 2, \ldots D)$	= traffic demand
$\boldsymbol{C_e}\ (e = 1, 2, \ldots.., E)$	= capacity
$\boldsymbol{e}$	= link weight metric
$\boldsymbol{\beta_e}$	= link metric bandwidth
$\boldsymbol{\beta} = (\beta_1, \beta_2, \ldots.., \beta_E)$	= link metric system
$\boldsymbol{P}$	= flow on path
$\boldsymbol{d}$	= traffic demand
$\boldsymbol{\beta}\ xdp\ (\beta)$	= triggered by the link metric system
$\sum_p xdp\ (\beta) = h_d, d = 1, 2, \ldots.D$	= level of dependency of traffic flows on β
$\boldsymbol{\beta}$	= link metric system
δ_{edp}	= link-path indicator
$\boldsymbol{p}$	= route for demand d
$\boldsymbol{y_{-e}}$ on link e	= link flow or link load
$\boldsymbol{y_{-e}}\ (\beta) \leq C_e, e = 1, 2, \ldots\ldots., E$	= flow link bounded task capacity
$\boldsymbol{\tau} = Max_{e=1,\ldots\ldots\ldots,E}\ \{y_{-e}(\beta)/C_e\}$	= maximum utilization over all links
$\boldsymbol{C_e}$	= link capacity
$\boldsymbol{A_{pd}}\ {}^{1}/_{(C_e - y_{-e})}$	= average packet delay
$\boldsymbol{y_{-e}} \leq C_e - {}^{1}/_{T}$	= link load capacity dependent event load
$\boldsymbol{X}$	= elements of set.
Vertex C_i is connected to vertex x_k if and only if $x_k \in C_i$, i.e., $\boldsymbol{C_1}$	$= \{x_1, x_2, x_3\}, C_2 = \{x_2, x_4, x_k\}$ and $C_n = \{x_{k-1}, x_{k+1}, x_p\}$.
$\boldsymbol{\mu s}$	= maximal flow from source vertex
$\boldsymbol{\mu t}$	= maximal flow from sink vertex
$\boldsymbol{C^{\wr}} = \{C_{i(1)}, C_{i(2)}, \ldots..C_{i(q)}, \}$	= visually impaired family sets.
$\boldsymbol{S_{d_c}}$	= *Sd card interface*
$\boldsymbol{I_rPe}$	= *IR Emiter*
$\boldsymbol{I_{as}Pd}$	= *IR Detector*
$\boldsymbol{A_{c_t}}$	= *Actuator controller*
$\sum f\ Pic$	= *microcontroller Plant*

APPENDIX II.

See Figure 24.

REFERENCES

[1] World Health Organization. (Oct. 14, 2021). *Blindness and Visual Impairment*. Accessed: Jul. 7, 2022. [Online]. Available: https://www.who.int/news-room/fact-sheets/detail/blindness-and-visual-impairment

[2] M. Hudec and Z. Smutny, "Ambient intelligence system enabling people with blindness to develop electrotechnical components and their drivers," *IEEE Access*, vol. 10, pp. 8539–8565, 2022.

[3] L. Cascone, M. Nappi, F. Narducci, and I. Passero, "DTPAAL: Digital twinning pepper and ambient assisted living," *IEEE Trans. Ind. Informat.*, vol. 18, no. 2, pp. 1397–1404, Feb. 2022.

[4] M. Irfan, H. Jawad, B. B. Felix, S. F. Abbasi, A. Nawaz, S. Akbarzadeh, M. Awais, L. Chen, T. Westerlund, and W. Chen, "Non-wearable IoT-based smart ambient behavior observation system," *IEEE Sensors J.*, vol. 21, no. 18, pp. 20857–20869, Sep. 2021.

[5] Z. Hong, M. Hong, N. Wang, Y. Ma, X. Zhou, and W. Wang, "A wearable-based posture recognition system with AI-assisted approach for healthcare IoT," *Future Gener. Comput. Syst.*, vol. 127, pp. 286–296, Feb. 2022.

[6] F. Firouzi, B. Farahani, and A. Marinšek, "The convergence and interplay of edge, fog, and cloud in the AI-driven Internet of Things (IoT)," *Inf. Syst.*, vol. 107, Jul. 2022, Art. no. 101840.

[7] D. Verma, K. R. Singh, A. K. Yadav, V. Nayak, J. Singh, P. R. Solanki, and R. P. Singh, "Internet of Things (IoT) in nano-integrated wearable biosensor devices for healthcare applications," *Biosensors Bioelectron. X*, vol. 11, Sep. 2022, Art. no. 100153.

[8] M. M. Islam, M. S. Sadi, K. Z. Zamli, and M. M. Ahmed, "Developing walking assistants for visually impaired people: A review," *IEEE Sensors J.*, vol. 19, no. 8, pp. 2814–2828, Apr. 2019.

[9] F. Özden, M. Özkeskin, E. Ar, and N. Yüceyar, "Gait assessment in shaped pathways: The test-retest reliability and concurrent validity of the figure of eight test and l test in multiple sclerosis patients without mobility aids," *Multiple Sclerosis Rel. Disorders*, vol. 65, Sep. 2022, Art. no. 103998.
[10] D.-C.-A. Lee, C. Meyer, E. Burton, S. Kitchen, C. Williams, S. W. Hunter, P. Suttanon, and K. D. Hill, "A survey of nurses, physiotherapists and occupational therapists in mobility care and gait aid use for hospital patients with dementia," *Geriatric Nursing*, vol. 44, pp. 221–228, Mar. 2022.
[11] P. Sedighi, M. H. Norouzi, and M. Delrobaei, "An RFID-based assistive glove to help the visually impaired," *IEEE Trans. Instrum. Meas.*, vol. 70, pp. 1–9, 2021, doi: 10.1109/TIM.2021.3069834.
[12] W.-J. Chang, L.-B. Chen, M.-C. Chen, J.-P. Su, C.-Y. Sie, and C.-H. Yang, "Design and implementation of an intelligent assistive system for visually impaired people for aerial obstacle avoidance and fall detection," *IEEE Sensors J.*, vol. 20, no. 17, pp. 10199–10210, Sep. 2020.
[13] J.-H. Kim, J.-E. Park, and J.-M. Lee, "3-D space visualization system using ultrasonic sensors as an assistive device for the blind," *IEEE J. Transl. Eng. Health Med.*, vol. 8, pp. 1–5, 2020.
[14] G. C. Bettelani, G. Averta, M. G. Catalano, B. Leporini, and M. Bianchi, "Design and validation of the readable device: A single-cell electromagnetic refreshable Braille display," *IEEE Trans. Haptics*, vol. 13, no. 1, pp. 239–245, Jan. 2020.
[15] A. Mancini, E. Frontoni, and P. Zingaretti, "Mechatronic system to help visually impaired users during walking and running," *IEEE Trans. Intell. Transp. Syst.*, vol. 19, no. 2, pp. 649–660, Feb. 2018.
[16] W. Y. Park, N. Shah, K. Shiraishi, and E. Vine, "Improving energy performance metrics to maximize the benefits of disruptive technologies," *Energy Res. Social Sci.*, vol. 89, Jul. 2022, Art. no. 102678.
[17] H. Majid, A. A. S. Atkins, A. S. Sorour, and R. J. Campion, "Ageing population supported by ambient-assisted living in the Kingdom of Saudi Arabia," in *Smart Home Technologies and Services for Geriatric Rehabilitation*, M.-A. Choukou and S. Syed-Abdul, Eds. New York, NY, USA: Academic, 2022, pp. 43–78.
[18] L. Tedesco Triccas, B. McLening, W. Hendrie, and G. Peryer, "Is there a standard procedure for assessing and providing assistive devices for people with neuro-disabling conditions in United Kingdom? A nation-wide survey," *Disability Health J.*, vol. 12, no. 1, pp. 93–97, Jan. 2019.
[19] Y. Singh, H. Raza, S. K. Sharma, and V. K. Bhat, "Computing basis and dimension of chloroquine and hydroxychloroquine by using chemical graph theory," *Polycyclic Aromatic Compounds*, early access, 2022. [Online]. Available: https://www.sciencedirect.com/org/science/article/abs/pii/S1040663822010880
[20] X. Li, H. Li, L. Cao, J. Liu, H. Xing, X. Huang, and Q. Gong, "Application of graph theory across multiple frequency bands in drug-Naïve obsessive-compulsive disorder with no comorbidity," *J. Psychiatric Res.*, vol. 150, pp. 272–278, Jun. 2022.
[21] R. Wu, F. Wang, P.-F. Yang, J. C. Gore, and L. M. Chen, "Graph theory analysis identified two hubs that connect sensorimotor and cognitive and cortical and subcortical nociceptive networks in the non-human primate," *NeuroImage*, vol. 257, Aug. 2022, Art. no. 119244.
[22] N. Bacanin, M. Sarac, N. Budimirovic, M. Zivkovic, A. A. AlZubi, and A. K. Bashir, "Smart wireless health care system using graph LSTM pollution prediction and dragonfly node localization," *Sustain. Comput., Informat. Syst.*, vol. 35, Sep. 2022, Art. no. 100711.
[23] W. Erb, "Graph signal interpolation with positive definite graph basis functions," *Appl. Comput. Harmon. Anal.*, vol. 60, pp. 368–395, Sep. 2022.
[24] L. Chennaz, D. Valente, N. Baltenneck, J.-Y. Baudouin, and E. Gentaz, "Emotion regulation in blind and visually impaired children aged 3 to 12 years assessed by a parental questionnaire," *Acta Psychol.*, vol. 225, May 2022, Art. no. 103553.
[25] M. A. Khatun, M. A. Yousuf, S. Ahmed, M. Z. Uddin, S. A. Alyami, S. Al-Ashhab, H. F. Akhdar, A. Khan, A. Azad, and M. A. Moni, "Deep CNN-LSTM with self-attention model for human activity recognition using wearable sensor," *IEEE J. Transl. Eng. Health Med.*, vol. 10, pp. 1–16, 2022.
[26] N. Besse, S. Rosset, J. J. Zárate, E. Ferrari, L. Brayda, and H. Shea, "Understanding graphics on a scalable latching assistive haptic display using a shape memory polymer membrane," *IEEE Trans. Haptics*, vol. 11, no. 1, pp. 30–38, Jan. 2018.
[27] R. P. Barros, A. M. F. Burlamaqui, S. O. Azevedo, S. T. D. L. Sa, L. M. G. Gonçalves, and A. A. R. S. D. S. Burlamaqui, "CardBot—Assistive technology for visually impaired in educational robotics: Experiments and results," *IEEE Latin Amer. Trans.*, vol. 15, no. 3, pp. 517–527, Mar. 2017.
[28] D. T. V. Pawluk, R. J. Adams, and R. Kitada, "Designing haptic assistive technology for individuals who are blind or visually impaired," *IEEE Trans. Haptics*, vol. 8, no. 3, pp. 258–278, Jul. 2015.
[29] A. K. Talukdar and M. K. Bhuyan, "Vision-based continuous sign language spotting using Gaussian hidden Markov model," *IEEE Sensors Lett.*, vol. 6, no. 7, pp. 1–4, Jul. 2022.
[30] A. Pergolini, C. Livolsi, E. Trigili, B. Chen, F. Giovacchini, A. Forner-Cordero, S. Crea, and N. Vitiello, "Real-time locomotion recognition algorithm for an active pelvis orthosis to assist lower-limb amputees," *IEEE Robot. Autom. Lett.*, vol. 7, no. 3, pp. 7487–7494, Jul. 2022.
[31] Z.-H. Chen, Y.-L. Yang, K.-W. Lin, P.-C. Sun, and C.-S. Chen, "Functional assessment of 3D-printed multifunction assistive hand device for chronic stroke patients," *IEEE Trans. Neural Syst. Rehabil. Eng.*, vol. 30, pp. 1261–1266, 2022.
[32] H. O. Edughele, Y. Zhang, F. Muhammad-Sukki, Q.-T. Vien, H. Morris-Cafiero, and M. O. Agyeman, "Eye-tracking assistive technologies for individuals with amyotrophic lateral sclerosis," *IEEE Access*, vol. 10, pp. 41952–41972, 2022.
[33] C. Chen, K. Zhang, Y. Leng, X. Chen, and C. Fu, "Unsupervised sim-to-real adaptation for environmental recognition in assistive walking," *IEEE Trans. Neural Syst. Rehabil. Eng.*, vol. 30, pp. 1350–1360, 2022, doi: 10.1109/TNSRE.2022.3176410.
[34] A. Ikpehai, B. Adebisi, K. M. Rabie, K. Anoh, R. E. Ande, M. Hammoudeh, H. Gacanin, and U. M. Mbanaso, "Low-power wide area network technologies for Internet-of-Things: A comparative review," *IEEE Internet Things J.*, vol. 6, no. 2, pp. 2225–2240, Apr. 2019.
[35] A. Subrahmannian and S. K. Behera, "Chipless RFID sensors for IoT-based healthcare applications: A review of state of the art," *IEEE Trans. Instrum. Meas.*, vol. 71, pp. 1–20, 2022.
[36] P. Fazio, M. Mehic, and M. Voznak, "An innovative dynamic mobility sampling scheme based on multiresolution wavelet analysis in IoT networks," *IEEE Internet Things J.*, vol. 9, no. 13, pp. 11336–11350, Jul. 2022.
[37] M. Mahyoub, A. S. H. Mahmoud, M. Abu-Amara, and T. R. Sheltami, "An efficient RPL-based mechanism for node-to-node communications in IoT," *IEEE Internet Things J.*, vol. 8, no. 9, pp. 7152–7169, May 2021.
[38] J. H. Anajemba, T. Yue, C. Iwendi, P. Chatterjee, D. Ngabo, and W. S. Alnumay, "A secure multiuser privacy technique for wireless IoT networks using stochastic privacy optimization," *IEEE Internet Things J.*, vol. 9, no. 4, pp. 2566–2577, Feb. 2022.
[39] A. L. de Oliveira, C. E. Capovilla, I. R. S. Casella, J. L. Azcue-Puma, and A. J. S. Filho, "Co-simulation of an SRG wind turbine control and GPRS/EGPRS wireless standards in smart grids," *IEEE/CAA J. Autom. Sinica*, vol. 8, no. 3, pp. 656–663, Mar. 2021.
[40] E. Sansano-Sansano, R. Montoliu, Ó. Belmonte-Fernández, F. J. Aranda, and F. J. Álvarez, "Continuous non-invasive assessment of gait speed through Bluetooth low energy," *IEEE Sensors J.*, vol. 22, no. 8, pp. 8183–8195, Apr. 2022.
[41] V. Therrien, H. Mellah, V. Boutin, and B. Sansò, "A large-scale simulator for NB-IoT," *IEEE Access*, vol. 10, pp. 68231–68239, 2022.
[42] S. Aguilar, D. S. W. La-Torre, A. Platis, R. Vidal, C. Gomez, S. Céspedes, and J. C. Zúñiga, "Packet fragmentation over SigFox: Implementation and performance evaluation of SCHC ACK-on-error," *IEEE Internet Things J.*, vol. 9, no. 13, pp. 11057–11070, Jul. 2022.
[43] L. Joris, F. Dupont, P. Laurent, P. Bellier, S. Stoukatch, and J.-M. Redouté, "An autonomous SigFox wireless sensor node for environmental monitoring," *IEEE Sensors Lett.*, vol. 3, no. 7, pp. 1–4, Jul. 2019.
[44] A. Lavric, A. I. Petrariu, and V. Popa, "Long range SigFox communication protocol scalability analysis under large-scale, high-density conditions," *IEEE Access*, vol. 7, pp. 35816–35825, 2019.
[45] R. Singh and Y. Chen, "Learning Gaussian hidden Markov models from aggregate data," *IEEE Control Syst. Lett.*, vol. 7, pp. 478–483, 2023.
[46] Q. Mascret, G. Gagnon-Turcotte, M. Bielmann, C. L. Fall, L. J. Bouyer, and B. Gosselin, "A wearable sensor network with embedded machine learning for real-time motion analysis and complex posture detection," *IEEE Sensors J.*, vol. 22, no. 8, pp. 7868–7876, Apr. 2022.
[47] K. Ren, H. Ahn, and M. Kamgarpour, "Chance-constrained trajectory planning with multimodal environmental uncertainty," *IEEE Control Syst. Lett.*, vol. 7, pp. 13–18, 2022.
[48] J. J. Garcia-Luna-Aceves, Z. Wang, H. R. Sadjadpour, and S. S. Karande, "Optimal unicast capacity of random geometric graphs: Impact of multi-packet transmission and reception," *IEEE J. Sel. Areas Commun.*, vol. 27, no. 7, pp. 1180–1191, Sep. 2009.

[49] Y. Zhou, J. Xiao, Y. Zhou, and G. Loianno, "Multi-robot collaborative perception with graph neural networks," *IEEE Robot. Autom. Lett.*, vol. 7, no. 2, pp. 2289–2296, Apr. 2022.
[50] A. D. P. D. Santos, A. H. G. Suzuki, F. O. Medola, and A. Vaezipour, "A systematic review of wearable devices for orientation and mobility of adults with visual impairment and blindness," *IEEE Access*, vol. 9, pp. 162306–162324, 2021.
[51] X. Hu, A. Song, Z. Wei, and H. Zeng, "StereoPilot: A wearable target location system for blind and visually impaired using spatial audio rendering," *IEEE Trans. Neural Syst. Rehabil. Eng.*, vol. 30, pp. 1621–1630, 2022.
[52] U. Masud, T. Saeed, H. M. Malaikah, F. U. Islam, and G. Abbas, "Smart assistive system for visually impaired people obstruction avoidance through object detection and classification," *IEEE Access*, vol. 10, pp. 13428–13441, 2022.
[53] M. A. Khan, P. Paul, M. Rashid, M. Hossain, and M. A. R. Ahad, "An AI-based visual aid with integrated reading assistant for the completely blind," *IEEE Trans. Human-Mach. Syst.*, vol. 50, no. 6, pp. 507–517, Dec. 2020.
[54] J. Tang, M. Sun, L. Zhu, M. Hu, M. Zhou, J. Zhang, Q. Li, and G. Zhai, "Design and optimization of an assistive cane with visual odometry for blind people to detect obstacles with hollow section," *IEEE Sensors J.*, vol. 21, no. 21, pp. 24759–24770, Nov. 2021.
[55] B. Jiang, J. Yang, Z. Lv, and H. Song, "Wearable vision assistance system based on binocular sensors for visually impaired users," *IEEE Internet Things J.*, vol. 6, no. 2, pp. 1375–1383, Apr. 2019.
[56] S. K. Jarraya, W. S. Al-Shehri, and M. S. Ali, "Deep multi-layer perceptron-based obstacle classification method from partial visual information: Application to the assistance of visually impaired people," *IEEE Access*, vol. 8, pp. 26612–26622, 2020.
[57] A. Buzachis, A. Celesti, A. Galletta, J. Wan, and M. Fazio, "Evaluating an application aware distributed Dijkstra shortest path algorithm in hybrid cloud/edge environments," *IEEE Trans. Sustain. Comput.*, vol. 7, no. 2, pp. 289–298, Apr. 2022.
[58] M. Pióro and D. Medhi, *Routing, Flow, and Capacity Design in Communication and Computer Networks—A Volume in the Morgan kaufmann Series in Networking*. Amsterdam, The Netherlands: Elsevier, 2004.
[59] M. Ismail, M. Islam, I. Ahmad, F. A. Khan, A. B. Qazi, Z. H. Khan, Z. Wadud, and M. Al-Rakhami, "Reliable path selection and opportunistic routing protocol for underwater wireless sensor networks," *IEEE Access*, vol. 8, pp. 100346–100364, 2020.
[60] J. Wang, X. Yu, R. Zong, and S. Lu, "Evacuation route optimization under real-time toxic gas dispersion through CFD simulation and Dijkstra algorithm," *J. Loss Prevention Process Ind.*, vol. 76, May 2022, Art. no. 104733.
[61] Y. Zhou and N. Huang, "Airport AGV path optimization model based on ant colony algorithm to optimize Dijkstra algorithm in urban systems," *Sustain. Comput., Informat. Syst.*, vol. 35, Sep. 2022, Art. no. 100716.
[62] E. Price and D. P. Woodruff, "Applications of the Shannon–Hartley theorem to data streams and sparse recovery," in *Proc. IEEE Int. Symp. Inf. Theory*, Cambridge, MA, USA, Jul. 2012, pp. 2446–2450.
[63] T. Myers. (2016). *Back to Basics: The Shannon-Hartley Theorem*. Accessed: Jul. 10, 2022. [Online]. Available: https://www.ingenu.com/2016/07/back-to-basics-the-Shannon-Hartley-theorem/
[64] A. AlAmmouri, J. G. Andrews, and F. Baccelli, "SINR and throughput of dense cellular networks with stretched exponential path loss," *IEEE Trans. Wireless Commun.*, vol. 17, no. 2, pp. 1147–1160, Feb. 2018.
[65] A. J. Ramadhan, "Wearable smart system for visually impaired people," *Sensors*, vol. 18, no. 3, p. 843, Mar. 2018.
[66] T. Bouguera, J. F. Diouris, J. J. Chaillout, R. Jaouadi, and G. Andrieux, "Energy consumption model for sensor nodes based on LoRa and LoRaWAN," *Sensors*, vol. 18, no. 2104, pp. 1–23, 2018.

KENNEDY CHINEDU OKAFOR (Senior Member, IEEE) received the Ph.D. degree in digital electronics and computer engineering from the University of Nigeria, Nsukka, Nigeria, in 2017. Previously, he worked with the National Agency for Science and Engineering Infrastructure (NASENI-ELDI-FMST), Nigeria, as a Senior Research and Development Engineer, from 2006 to 2014, before joining as a Teaching Researcher at the Department of Electrical and Electronic Engineering. He is currently working in mechatronics engineering with the Federal University of Technology-Owerri, Owerri, Nigeria. He has various certification exposure, including CCNA, CCNP, CompTIA A+, Server+, DevNet, and IBM Cloud certifications. He has published in reputable/top impact factor venues, including IEEE, Wiley, Elsevier, Springer, IGI-Global, and Taylor & Francis. He has served on over 50 Technical committees (IEEE workshops/conferences, Tetfund, National Assembly, and various consortiums). He is the Chair of IEEE Consultants Network, Nigeria. He is also a Senior Research Associate with the Department of Electrical and Electronic Engineering Science, University of Johannesburg, South Africa. He is also an Adjunct Facilitator with the World Bank Africa Center of Excellence for Sustainable Power and Energy Development (ACE-SPED), University of Nigeria. He collaborates with Cisco Systems NetAcad, IBM Global University Program, Africa. He is a fellow of the African Scientific Institute, USA. His research interests include AI, cloud data center designs, cyberphysical systems, green energy analytics, and 4IR domains. He has organized several IEEE conferences in Africa and serving as a keynote speaker in IEEE conferences in Asia and Africa. He has reviewed over 300 papers, managed over 285 editorial tasks (both in Scopus & Web of Science), and has presented papers at both Int'l and local conferences. He is also on the editorial review board of more than 15 high impact factor journals in USA, U.K., Asia, and Africa. He has presented over 50 invited talks (keynotes, tutorials, and seminars). He has attracted over $2,160,756 research/project grant portfolio in Nigeria, and has led most IEEE, government, university, and industrial funded projects with excellent impacts, between 2019 and 2022. He is currently the Chair of IEEE Consultants Networks AG, Nigeria, the Subsection Chair of IEEE South-East Nigeria, the Project Manager of FUTO CISCO Academy, Nigeria, and the Chair of the MSR-Laboratories, FUTO.

OMOWUNMI MARY LONGE (Senior Member, IEEE) received the B.Eng. and M.Eng. degrees in electrical and electronics engineering from the Federal University of Technology Akure, Akure, Ondo, Nigeria, in 2001 and 2011, respectively, and the Doctor of Engineering (D.Eng.) degree in electrical and electronic engineering science from the University of Johannesburg, South Africa, in 2017. She is currently a Senior Lecturer and the Chair of the Smart Power and Energy Research Group, Department of Electrical and Electronic Engineering Science, University of Johannesburg. She has published more than 40 papers at refereed journals and conferences. Her research interests include smart secured systems, renewable energy technologies, microgrid design, electromobility, energy poverty, distributed energy storage, demand side management, demand response, smart energy management, energy efficiency, distributed energy generation, rural electrification, energy and gender poverty nexus, energy and power system analysis and dynamics, smart city energy and transportation, energy 4.0 systems, and electromobility. She is also a reviewer of ISI-listed journals and refereed professional conferences. She has served as a member of technical program committee for local and international conferences. She is a Senior Member of the South African Institute of Electrical Engineers (SAIEE). She also serves as the Vice Chair of IEEE PES Women in Power Executive Committee (2022–2023), the Education Chair of IEEE Smart Village—Africa Working Group (2022–2023), a member of IEEE PES Diversity and Inclusion Committee, and a member of IEEE PES LRP Education Sub-Committee. She is also a member of Nigeria Society of Engineers (NSE), the Association of Professional Women Engineers of Nigeria (APWEN), and the Society of Women Engineers (SWE), USA. She is also registered with the Engineering Council of South Africa (ECSA).